AD-A115 796 SCIENTIFIC RESEARCH ASSOCIATES INC GLASTONBURY CT F/G 20/4
NAVIER-STOKES COMPUTATIONS OF AFT END FLOW FIELDS.(U)
MAY 82 B C WEINBERG, H MCDONALD, S J SHAMROTH DAAG29-79-C-0003
UNCLASSIFIED ARO-15905.1-EG NL

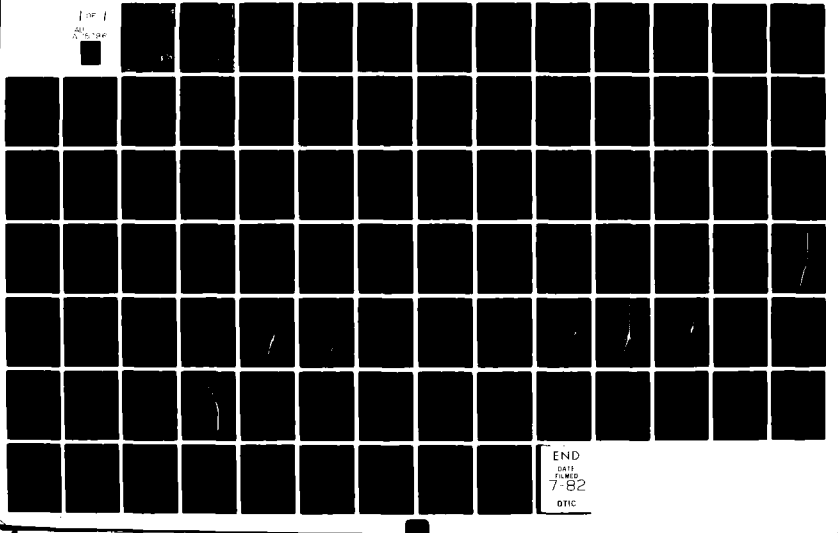

NAVIER-STOKES COMPUTATIONS OF AFT END FLOW FIELDS

FINAL REPORT

B. C. Weinberg
H. McDonald
S. J. Shamroth

May 1982

U. S. Army Research Office

Contract DAAG29-79-C-0003

Prepared by
Scientific Research Associates, Inc.
P. O. Box 498
Glastonbury, CT 06033

SECURITY CLASSIFICATION OF T 'AGE (When Data Entered)

REPORT DOCUMENTATION PAGE

READ INSTRUCTIONS BEFORE COMPLETING FORM

1. REPORT NUMBER	2. GOVT ACCESSION NO. AD-A115 996 / 3. RECIPIENT'S CATALOG NUMBER
4. TITLE (and Subtitle) Navier-Stokes Computations of Aft End Flow Fields	5. TYPE OF REPORT & PERIOD COVERED Final Report 15 Dec 1978 - 14 March 1982
	6. PERFORMING ORG. REPORT NUMBER
7. AUTHOR(s) Bernard C. Weinberg, Henry McDonald, Stephen J. Shamroth	8. CONTRACT OR GRANT NUMBER(s) DAAG29-79-C-0003
9. PERFORMING ORGANIZATION NAME AND ADDRESS Scientific Research Associates, Inc. P.O. Box 498 Glastonbury, CT 06033	10. PROGRAM ELEMENT, PROJECT, TASK AREA & WORK UNIT NUMBERS
11. CONTROLLING OFFICE NAME AND ADDRESS U.S. Army Research Office Post Office Box 12211 Research Triangle Park, NC 27709	12. REPORT DATE May 1982
	13. NUMBER OF PAGES
14. MONITORING AGENCY NAME & ADDRESS(if different from Controlling Office)	15. SECURITY CLASS. (of this report) Unclassified
	15a. DECLASSIFICATION/DOWNGRADING SCHEDULE

16. DISTRIBUTION STATEMENT (of this Report)

Approved for Public Release; Distribution Unlimited

17. DISTRIBUTION STATEMENT (of the abstract entered in Block 20, if different from Report)

N/A

18. SUPPLEMENTARY NOTES

The view, opinions, and/or findings contained in this report are those of the author(s) and should not be construed as an official department of the Army position, policy, or decision unless so designated by other documentation.

19. KEY WORDS (Continue on reverse side if necessary and identify by block number)

Multidimensional Implicit Numerical Method
Navier-Stokes Equations
Aft End Flow Field
Boattail Geometry
Time-Dependent Adaptive Grid

20. ABSTRACT (Continue on reverse side if necessary and identify by block number)

In this report the development of a Navier-Stokes code to solve the aft end flow field of missile type configurations is presented. The consistently split linearized block implicit method of McDonald and Briley is employed in modified form to handle L-shaped domains with sharp reentrant corners. Appropriate boundary conditions are applied for the supersonic flow in particular at the outer boundary so that waves generated within the flow field are allowed to pass out of the computational domain without reflecting back into it. An adaptive grid option has been incorporated into the code and has been exercised by

DD FORM 1 JAN 73 1473 EDITION OF 1 NOV 65 IS OBSOLETE

Unclassified

SECURITY CLASSIFICATION OF THIS PAGE (When Data Entered)

following the shear layer in a model backstep problem. Results are presented for the supersonic turbulent flow over a nozzle boattail configuration with and without jet exhaust and the results are compared with experiment. Calculations of the 2-D turbulent supersonic flow over a right angle back step with shear layer reattachment on a 20° ramp are also shown, and compared with experiments. The computation shows the qualitative physical behavior of the flows and there is generally good agreement with the experimental velocity profiles through most of the free shear layer and the ramp reattachment zone.

TABLE OF CONTENTS

INTRODUCTION

The flow field in the aft-end region of an aerodynamic vehicle is a complex phenomenon which has important ramifications for the vehicle performance. For example, under many conditions aft-body drag represents a significant fraction of the total drag occurring on a jet engine nacelle and this portion of the drag can be radically influenced by the nacelle boattail shape. An analysis capable of giving accurate predictions of the flow field in this region, including off-design operation, could play an important role in the boattail design process particularly from the point of view of optimizing the trade-off between aft-end drag and boattail weight. The aft-end flow field problem is also very important in transonic flow situations where improved design can lead to a delayed transonic drag rise. In a different application the problem also becomes significant when considering the effect of a propulsive jet plume on missile aerodynamics. In this case the major interest centers on missile stability and control surface effectiveness. Under some actual flight conditions the jet plume may cause separation and/or significant flow field changes upstream of the missile base. These in turn can result in catastrophic missile pitch up or loss of accuracy. However, loss of control surface effectiveness need not be always detrimental; it can be an advantage in the transonic portion of the missile boost phase. Under transonic boost phase conditions loss of effectiveness may lead to a decrease in missile wind sensitivity which is a desirable effect during the boost phase. Thus, in the case of a missile, loss of control surface effectiveness during the transonic boost phase combined with a high degree of control surface effectiveness in supersonic flow may be the desired design goal. In addition, the recirculating gases can of course pose a danger because of their high temperature. Should these hot gases come in contact with an unprotected surface, catastrophic failure could result.

The aft-end flow problem has been the subject of numerous experimental and theoretical investigations. Most of these were concerned with the flow field about a back step or base with little or no bleed. However, studies more germane to the present problem also have been performed. These include a series of experimental efforts aimed at investigating the missile plume effect problem some of which have been reported in the bibliography compiled by Batiuk (Ref. 1), the isolated afterbody problem which was investigated experimentally by Shrewsbury (Ref. 2) and the jet plume problem which was investigated experimentally by Strike (Ref. 3) and Alpineri and Adams (Ref. 4) and Galigher, et al (Ref. 5).

Although Refs. 1, 3 and 4 present experiments aimed directly at the jet plume problem, it should be noted that accurate wind tunnel simulations of the jet plume flow field are difficult to attain for two reasons. The first problem which arises is that of jet exhaust simulation. In general, the jet exhaust is represented either by a solid body jet simulation or by passing either hot or cold flow through a model exhaust. At present it is an open question as to how well these techniques simulate the actual flow at flight Reynolds numbers. In an investigation of missile configurations Burt (Ref. 6) concluded that his plume simulators give approximately the same afterbody pressure distributions as a real plume. Nevertheless the jet simulation problem is a difficult one to resolve in general. Secondly, scale effects due to the lack of simulation of both the aft-end boundary layer and the free mixing layer may cause uncertainty in the experimental results. This is particularly true in the transonic regime where viscous-inviscid interacting effects play a major role in determining the flow field, and where the interaction effects may be very sensitive to the viscous layer thicknesses. These potential problems associated with wind tunnel testing show that theoretical prediction procedures are a valuable compliment to existing experimental tools.

As in the case of experiments, most theoretical analyses of the aft-end flow field have been confined to back steps or base flows without bleed. In addition most analyses have been primarily concerned with predicting overall flow field quantities such as base pressure, pressure distribution during recompression, length of the recirculation region, etc., rather than a detailed picture of the flow field behavior. These analyses for the most part are based upon 'critical point' methods (e.g., Refs. 7-11) or 'component analysis' methods (e.g., Refs. 12-15). Since the analyses are concerned with the overall rather than the detailed nature of the flow field, they usually have relied heavily upon boundary layer integral methods, mixing analyses and/or semi-empirical relationships. Nevertheless, these base pressure analyses have been remarkably successful in predicting certain of the overall flow field characteristics. In addition, they are usually straightforward to implement and require relatively little computer time. In supersonic external flow where the major concern is base pressure or centerline recompression pressure rise for back step or base configurations with simple geometry and little or no bleed, these rapid techniques may be quite adequate. However, the inherent quantities which make the procedures rapid and easy to implement also make them unsuitable for entirely subsonic flow and for predicting details of recirculating flow and make them questionable for cases

in which large bleed, complex geometries, etc., are important. For example, these methods could not be expected to predict the details of a transonic jet plume interaction flow field particularly if the underexpanded propulsive jet were to cause separation of the boundary layer at some location on the afterbody. Therefore, if a detailed description of the aft-end flow is desired, an alternative procedure must be used.

Recently, the advent of larger and faster computers and more efficient numerical techniques have led to more detailed investigations of vehicle aft-end flow fields. Several investigations have used the Navier-Stokes equations to predict backstep and base flow fields (e.g., Refs. 16-21), and only recently have the Navier-Stokes equations have not generally been applied to the full jet-plume interaction flow field problem (Ref. 22). In addition, the subsonic boattail problem has been investigated by Rom and Bober (Ref. 23) who used an equivalent body to represent the wake. Fong (Ref. 24) combined the Chapman-Korst analysis with a method of characteristics analysis to study the jet plume problem which included the effect of plume induced boundary layer separation. Sinha, Zakkay and Erdos (Ref. 25) developed an inviscid solution to the underexpanded jet plume. More recently Grossman and Melnik (Ref. 26) modeled the transonic jet plume problem by interacting three separate analyses. The jet plume is calculated using the inviscid method of Salas (Ref. 27); the external transonic flow is calculated using an inviscid procedure based upon the work of Murman and Cole (Ref. 28) and Jameson (Ref. 29) and the viscous boundary layer and mixing layer are calculated using the integral procedure of Green, Weeks and Broman (Ref. 30). Insofar as predicting flow details and interaction effects, the method of Ref. 26 represents a significant improvement over earlier 'component analysis' and 'critical point' methods. (It should be noted that these latter methods were developed primarily to predict supersonic base pressure and recompression pressure distributions in zero and small bleed cases and in these situations the methods seem to perform quite well.) However, as Grossman and Melnik noted in Ref. 26, their analysis does make compromises in the treatment of viscous effects. In particular the method uses an integral boundary layer and mixing length analysis and such integral analyses are inherently limited by their profile assumptions. Although the method matches viscous and inviscid regions along the displacement surface in regions of small or moderate pressure gradient, displacement surface matching was found to be unstable in this procedure in regions of strong pressure gradient. Therefore, the viscous and inviscid flows

were matched along curve fits joining the displacement surfaces on either side of a strong pressure gradient region. In addition, the method ignores normal pressure gradients in the viscous regions and does not rigorously treat either the possible boundary layer separation on the boattail or regions of flow reversal.

In the present report we focus directly on the region of the flow where viscous-inviscid interaction are important. This region is sketched in Fig. 1. Consider the interaction of an under expanded propulsive jet with a supersonic flow over a boattail shaped body. The Reynolds number is assumed sufficiently high so that the approach boundary layer is turbulent. As the fluid flows over the boattail it will undergo a gradual expansion, up to some point upstream of the boattail base juncture where the presence of the jet will first be sensed. The location of this point depends in general upon the free stream and jet conditions as well as the geometry of the boattail.

In the region of upstream influence on the shoulder of the boattail the flow will compress rapidly forming a compression wave that will coalesce into a shock. The severe adverse pressure gradient that is generated in this process will lead to flow separation and the formation a recirculation zone. Immediately downstream of the base, the flow will undergo a rapid expansion, and thereafter recompress with the formation of the recompression shock.

Special consideration must be given to the computational domain which encompasses this strong interaction region. In Fig. 2 a schematic of the computational domain is presented. The bounding boundaries of the region of interest forms an L-shaped domain containing a sharp reentrant corner at point h.

The present effort considers only supersonic inflow and supersonic outflow boundaries for simplicity and since the amount of upstream influence in the (under-expanded) propulsive jet is expected to be minor the upstream conditions for the calculation within the nozzle are applied at the nozzle exit plane (line a-b of Fig. 2). Consideration of subsonic inflow and subsonic exit conditions is conceptually simple but probably would require a larger domain and could be the subject of a later investigation. The upstream conditions for the flow over the boattail are applied upstream of the nozzle exit plane so as to allow calculation of possible boattail separation effects (line c-d). The outer boundary conditions for the external flow is taken along a line parallel to the nozzle centerline which is far enough removed from the nozzle so as to allow application of freestream boundary conditions (line d-e) and keep spurious shock and/or Mach reflections from the boundary from impinging on regions of interest. Finally, the outflow

boundary of the present region of interest is taken downstream of the recirculation zone and weak streamwise derivative boundary conditions are applied along this line (line e-f). The solution at the downstream boundary could be used as inflow boundary conditions for a conventional viscous or inviscid procedure which could be used to predict the downstream "far" flow field.

Since the computatonal domain is L-shaped, standard solution algorithms must be modified to allow for efficient computations. Furthermore, the reentrant sharp corner is a geometrically singularity in the flow field, and must, therefore, be treated appropriately. A fuller discussion of these matters will be given later in this report.

Under the present effort a local flow field analysis is considered. This detailed solution then could be joined either to inviscid solutions or viscous forward marching solutions, as appropriate, in an interactive manner to determine the entire flow field. For supersonic bounding flows the matching of the detailed Navier-Stokes solution to the external flow is quite straightforward, provided of course that all regions of upstream influence of downstream disturbances are contained within the Navier-Stokes solution domain. For subsonic or transonic bounding flows the transient interacting technique of Briley and McDonald (Ref. 31) would be used, either as a linearized correction to the external stream or as a matching surface for a time or relaxation step in an inviscid flow calculation.

The procedure that is used in this effort is the Multidimensional Implicit Nonlinear Time-Dependent (MINT) procedure of Briley and McDonald (Ref. 32). This represents an accurate, efficient numerical procedure for solving the Navier-Stokes equations. The procedure was originally developed for laminar duct flow and was subsequently applied to turbulent duct flow by Briley, McDonald and Gibeling (Ref. 33). It has since been applied to the three-dimensional combustor flow problem by Gibeling, McDonald and Briley (Ref. 34). This procedure represents a well-proven and well-exercised method of solving the Navier-Stokes equations.

The MINT procedure has been previously described in Refs. 32 and 33, and consequently only a brief outline will be given here and the scheme presented in detail in Appendix B. The method can be briefly outlined as follows: The governing equations are replaced by an implicit time difference approximation, optionally a backward difference or Crank-Nicolson scheme. Terms involving nonlinearities at the implicit time level are linearized by Taylor expansion about the solution at the known time level, and spatial difference approximations are introduced. The result is a system of multidimensional coupled (but linear) difference equations for the dependent variables at the unknown or implicit time level. To solve these difference equations, the Douglas-Gunn (Ref. 35) procedure for

generating alternating direction implicit (ADI) schemes as perturbations of fundamental implicit difference schemes is introduced. This technique leads to systems of coupled linear difference equations having narrow block-banded matrix structures which can be solved efficiently by standard block-elimination methods.

The method centers around the use of a formal linearization technique adapted for the integration of initial-value problems. The linearization technique, which requires an implicit solution procedure, permits the solution of coupled nonlinear equations in one space dimension (to the requisite degree of accuracy) by a one-step noniterative scheme. Since no iteration is required to compute the solution for a single time step, and since only moderate effort is required for solution of the implicit difference equations, the method is computationally efficient; this efficiency is retained for multidimensional problems by using ADI techniques. The method is also economical in terms of computer storage, in its present form requiring only two time-levels of storage for each dependent variable. Furthermore, the ADI technique reduces multidimensional problems to sequences of calculations which are one-dimensional in the sense that easily-solved narrow block-banded matrices associated with one-dimensional rows of grid points are produced. Consequently, only these onc-dimensional problems require rapid-acess storage at any given stage of the solution procedure, and the remaining flow variables can be saved on auxiliary storage devices if desired. A more complete description of the linearization technique, the alternating direction technique and the solution procedure is presented in Appendix B.

THEORETICAL ANALYSIS

Governing Equations

In this section the governing equations are presented in vector form for a two-dimensional flow. The resulting Jacobian transformed governing conservation equations in cylindrical polar coordinates are given in Appendix A. It is convenient for turbulent flows to formally eliminate density fluctuations. This can be accomplished by using the mass weighted or Favre average (Ref. 36). The governing equations are then identical to the laminar equations with the flow variables being taken as mean quantities and viscosity being taken as the sum of the molecular viscosity μ, and the turbulent viscosity μ_T. The resulting equations are

Continuity

$$\frac{\partial \rho}{\partial t} - \nabla \cdot \rho \vec{u} = 0 \tag{1}$$

Momentum

$$\frac{\partial \rho \vec{u}}{\partial t} + \nabla \cdot (\rho \vec{u} \vec{u}) = -\nabla p + \nabla \cdot (\bar{\bar{\pi}} + \pi^T) \tag{2}$$

In the above equation $\bar{\bar{\Pi}}$ and Π^T are the average and turbulent stress tensor respectively.

Energy Equation

In the present formulation it is desirable to write the energy equation in terms of the static enthalpy h because of simplifications in the turbulence time averaging, viz.

$$\frac{\partial \rho h}{\partial t} + \nabla \cdot (\rho \vec{u} h) = -\nabla \cdot (\bar{\bar{q}} + \vec{q}^T) + \frac{\mathcal{D}p}{\mathcal{D}t} + \Phi + \rho \bar{\epsilon} \tag{3}$$

where Φ is the mean flow dissipation defined in Eq. (10) and $\vec{\epsilon}$ is the turbulence kinetic energy dissipation rate (cf. Eq. (20)).

Turbulence Kinetic Energy Equation

In the present work a turbulence kinetic energy equation and a specified length scale equation have been utilized. Following the derivations of (Refs. 37 - 38) and Ref. (39), one obtains

$$\frac{\partial(\rho k)}{\partial t} + \nabla\cdot(\rho\vec{U}k) = \nabla\cdot\left(\frac{\mu_T}{\sigma_k}\nabla k\right) \tag{4}$$

$$+ \left\{\mu_T\left[2\mathbb{D}:\mathbb{D} - \frac{2}{3}(\nabla\cdot\vec{U})^2\right] - \frac{2}{3}\rho k\nabla\cdot\vec{U} - \rho\epsilon\right\}$$

and k is the turbulence kinetic energy

$$\bar{k} = \frac{1}{2}\overline{\vec{u}'\cdot\vec{u}'} \tag{5}$$

Stress Tensors

The stress tensor assuming a Newtonian fluid is

$$\bar{\bar{\pi}} = 2\mu\mathbb{D} - \left(\frac{2}{3}\mu - K_B\right)\nabla\cdot\vec{U}\,\mathbb{I} \tag{6}$$

where K_B is the bulk viscosity coefficient and is the deformation tensor, i.e.

$$\mathbb{D} \equiv \frac{1}{2}\left[(\nabla\vec{U}) + (\nabla\vec{U})^T\right] \tag{7}$$

The turbulent flow stress tensor is modeled using an isotropic eddy viscosity formulation, i.e.,

$$\pi^T = -\bar{\bar{\rho}}\,\overline{\vec{u}'\vec{u}'} = 2\mu_T\mathbb{D} - \frac{2}{3}(\mu_T\nabla\cdot\vec{U} + \bar{\bar{\rho}}\bar{k})\,\mathbb{I} \tag{8}$$

where $\bar{k}$ is the turbulence kinetic energy, Eq. (5). The turbulent viscosity μ_T must be determined using a suitable turbulence model.

Heat Flux Vectors

The mean heat flux vector $\vec{\bar{\bar{q}}}$ and the turbulent heat flux vector $\vec{q}^T$ may be written as

$$\vec{\bar{\bar{q}}} = -\bar{\bar{\kappa}}\left[\nabla\bar{\bar{T}}\right] \tag{9}$$

$$\vec{q}^T = -\kappa^T\left[\nabla\bar{\bar{T}}\right] \tag{10}$$

where $\bar{\bar{\kappa}}$ is the mean thermal conductiveity, and κ^T is a turbulent conductivity,

Mean Flow Dissipation

The mean flow dissipation term appearing in the energy equation, Eq. (3), is defined as

$$\Phi = 2\mu \mathbb{D} : \mathbb{D} - \left(\frac{2}{3}\mu - K_B\right)(\nabla \cdot \vec{U})^2 \tag{11}$$

In the present analysis Eqs. (1-4) are solved in conjunction with Eqs. (6-10) and the constitutive relations for μ, μ_T, K_B, $\bar{\bar{\kappa}}$ and κ^T, which are given in the subsequent section.

Constitutive Relations

The necessary constitutive relations include an equation of state, a caloric equation of state, a turbulence length scale distribution, the molecular viscosity and thermal conductivity,

Equation of State

The equation of state is that of a perfect gas

$$P = \rho RT \tag{12}$$

where R is the gas constant,

The caloric equation of state is taken as

$$e = c_v T \tag{13}$$

where c_v would be dependent on the gas composition, but not temperature. We may also define the static enthalpy as

$$h = c_p T \tag{14}$$

where c_p, the specific heat at constant pressure is not a function of temperature. In the calculations presented in this report c_p and c_v were taken as constants.

Molecular Viscosity, Bulk Viscosity, and Thermal Conductivity

The molecular viscosity for the gas is determined from Sutherland's law,

$$\frac{\mu}{\mu_0} = \left(\frac{T}{T_0}\right)^{3/2} \frac{T_0+S_1}{T+S_1} \tag{15}$$

where $S_1 = 110°K$ for air.

The bulk viscosity will be assumed to be zero at present,

$$K_B = 0 \tag{16}$$

The thermal conductivity may be determined from a relation similar to Sutherland's law, e.g.,

$$\frac{\kappa}{\kappa_0} = \left(\frac{T}{T_0}\right)^{3/2} \frac{T_0+S_2}{T+S_2} \tag{17}$$

where $S_2 = 194°K$ for air.

Turbulence Model Relations

The turbulent viscosity introduced in Eq. (8) is obtained from the Prandtl-Kolmogorov relation, viz.

$$\mu_T = c_\mu \frac{\rho k^2}{\bar{\epsilon}} \tag{18}$$

and the dissipation rate is given by

$$\bar{\epsilon} = c_\mu^{3/4} \frac{\bar{k}^{3/2}}{\ell} \tag{19}$$

where the turbulence length scale, ℓ, must be specified consistent with the expected turbulence structure in the flow. Following Ref. 40 the constant σ_k will be taken as

$$\sigma_k = 1.0 \tag{20}$$

There are two options available for modeling the turbulence near a wall. In the first, grid point resolution normal to the wall must be sufficient to define the viscous sublayer, in which case the boundary conditions are relatively straightforward. However, the difficulty with this approach is that the physics of low Reynolds number (transitional) turbulence must be modeled in a reasonable manner by the governing turbulence equations (e.g., Jones and Launder, Ref. 40). An alternative approach is to employ a less refined mesh and force the turbulence variables to yield values consistent with a boundary layer wall function formulation at the first grid point away from the wall. The difficulty with this approach is that the validity of the wall function formulation is questionable under the flow conditions of the viscous inviscid interaction problem. A transition model, which was successfully used by Shamroth and Gibeling (Ref. 41) in a time dependent airfoil flow field analysis, has been implemented in the computer code. The analysis of Ref. 41 follows the integral turbulence energy procedure of Refs. 42 - 44 by utilizing a turbulence function a_1, where

$$a_1 = c_\mu^{1/2}/2 \tag{21}$$

and a_1 is taken as a function of a turbulence Reynolds number of the form

$$a_1 = a_0\left[\frac{f(R_\tau)}{100}\right] \Big/ \left\{1.0 + 6.66\, a_0\left[\frac{f(R_\tau)}{100} - 1\right]\right\} \tag{22}$$

where

$$a_0 = .0115$$

$$f(R_\tau) = 100.\, R_\tau^{0.22} \qquad R_\tau \le 1$$

$$f(R_\tau) = 68\,1 R_\tau + 614.3 \qquad R_\tau \ge 40 \tag{23}$$

and a cubic curve was fit for values of R_τ between 1 and 40. As previously discussed, Ref. 42 - 44 utilized an integral form of the turbulence kinetic energy and, therefore, R_τ was defined as an average value.

$$R_\tau = \frac{1}{\delta}\int_0^{\delta} \nu_T\, dy \Big/ \frac{1}{\delta}\int_0^{\delta_s} \nu\, dy_s \tag{24}$$

In the present effort R_τ was defined as the local ratio of turbulent to laminar viscosity, a_1 was evaluated via Eq. 22 and C_μ related to a_1 via Eq. 21.

The effective viscosity is defined as the sum of the laminar and turbulent viscosities

$$\mu_{eff} = \mu + \mu_T \tag{25}$$

The effective conductivity will be modeled using an effective Prandtl number obtained from knowledge of turbulent flows of gases and gas mixtures, i.e.,

$$\kappa_{eff} = \bar{\kappa} + \kappa^T = \frac{c_p \mu_{eff}}{Pr_{eff}} \tag{26}$$

and $Pr_{eff} = 0.9$ for air.

Turbulence Length Scale

The near wall region mixing length is obtained from the McDonald's model (Ref. 45) with Van Driest damping (Ref. 46),

$$\ell = \ell_\infty \tanh\left[\frac{\kappa y}{\ell_\infty}\right]\left[1 - \exp(-y^+/A^+)\right] \tag{27}$$

where κ is the von Karman constant and A^+ is the van Driest damping coefficient,

$$\kappa = 0.4$$

$$A^+ = 26.0$$

and $\ell_\infty = .09\delta$.

The nondimensional distance y^+ is defined as

$$y^+ = y\left(\frac{\rho U_\tau}{\mu}\right) \tag{28}$$

and the friction velocity u_τ in the present analysis is taken as

$$U_\tau = \left(\frac{\tau_\ell}{\rho}\right)^{1/2} \tag{29}$$

where the local shear stress τ_ℓ is obtained from

$$\tau_\ell = (2\mathbb{D}:\mathbb{D})^{1/2} \tag{30}$$

Note that for small y the tanh function in Eq. (27) reduces to ky while for large y it approaches ℓ_∞.

A more detailed description of the actual turbulence models used for the computation and their effect on the computation will be given in the discussion section of the paper.

COORDINATE TRANSFORMATION

The set of governing partial differential equations which model the physical processes was presented in the previous section. For generality these equations were written in vector notation; however, before these equations can be incorporated into a computer code, a coordinate system must be chosen. The governing equations can then be cast in a form reflecting the choice of the coordinate system. The coordinate system for a nozzle boat-tail geometry must allow for the boat-tail body to be a coordinate line, the nozzle exit plane to be a straight line and it should have the flexibility of clustering points in regions of large shear. Another feature of the coordinate system should be its ability to adapt the mesh distribution as regions of large shear develop during the calculation, i.e. be time dependent. In order to permit consistent calculation of the Jacobian in a moving coordinate system, the governing equations should be transformed with a Jacobian transformation of the form

$$y^j = y^j(\bar{x}_1, \bar{x}_2, \bar{x}_3, t) \qquad (31)$$

$$\tau = t$$

where $(\bar{x}_1, \bar{x}_2, \bar{x}_3)$ are the original coordinates (cf. Ref. 47). In cylindrical polar coordinates $(\vec{x}_i)$ would correspond to (r, θ, z). The velocity components remain the components, (U_1, U_2, U_3) in the $(\bar{x}_1, \bar{x}_2, \bar{x}_3)$ coordinate directions respectively. The new independent variables y^j are the computational coordinates in the transformed system. The coordinate system requirements for the problem under consideration may be represented by a subset of the general transformation, Eq. (31)

$$y^1 = y^1(x_1, x_3, t)$$

$$y^2 = y^2(x_2) \qquad (32)$$

$$y^3 = y^3(x_1, x_3, t)$$

which is a general axisymmetric time-dependent transformation. For the nozzle and boattail geometry which is axisymmetric, Eq. (32) reduces to $y^2 = \bar{x}_2$ and all derivatives $\partial/\partial y^2$ are assumed to be zero.

Application of the Jacobian transformation requires expansion of the temporal and spatial derivatives using the chain rule, i.e.,

$$\frac{\partial \phi}{\partial t} = \frac{\partial \phi}{\partial \tau} + \sum_{j=1}^{3} y^j_{,t} \frac{\partial \phi}{\partial y^j} \tag{33}$$

and

$$\frac{\partial \phi}{\partial \bar{x}_i} = \sum_{j=1}^{3} y^j_{,i} \frac{\partial \phi}{\partial y^j} \tag{34}$$

where

$$y^j_{,t} \equiv \frac{\partial y^j}{\partial t}$$

$$y^j_{,i} \equiv \frac{\partial y^j}{\partial \bar{x}_i} \tag{35}$$

The relations Eq. (33-35) are first substituted into the governing equations (1-4) written in Cartesian or cylindrical polar coordinates. Then the resulting equations are multiplied by the Jacobian determinant of the inverse transformation,

$$J = \frac{\partial(\bar{x}_1, \bar{x}_2, \bar{x}_3)}{\partial(y^1, y^2, y^3)} = \begin{vmatrix} \frac{\partial \bar{x}_1}{\partial y^1} & \frac{\partial \bar{x}_1}{\partial y^2} & \frac{\partial \bar{x}_1}{\partial y^3} \\ \frac{\partial \bar{x}_2}{\partial y^1} & \frac{\partial \bar{x}_2}{\partial y^2} & \frac{\partial \bar{x}_2}{\partial y^3} \\ \frac{\partial \bar{x}_3}{\partial y^1} & \frac{\partial \bar{x}_3}{\partial y^2} & \frac{\partial \bar{x}_3}{\partial y^3} \end{vmatrix} \tag{36}$$

and the equations are cast into a "semi-strong" conservation form (Ref. 56) using the following relations,

$$\sum_{j=1}^{3} \frac{\partial (J y^j_{,i})}{\partial y^j} = 0 \tag{37}$$

and

$$\frac{\partial J}{\partial \tau} + \sum_{j=1}^{3} \frac{\partial J y^{j}_{,t}}{\partial y^{j}} = 0 \tag{38}$$

The semi-strong conservation form implies that all factors involving the radial coordinate $r = \bar{x}_1$ remain as they were before the Jacobian transformation. The resulting equations are presented in Appendix B.

The geometric relations Eq. (37-38) may be obtained from the transformation relations for $J\dot{y}^{j}_{,t}$ and $J\dot{y}^{j}_{,i}$ in terms of the inverse transformation derivatives (e.g., Ref. 44),

$$\begin{aligned}
J\dot{y}^{1}_{,1} &= \bar{x}_{2,2}\,\bar{x}_{3,3} - \bar{x}_{2,3}\,\bar{x}_{3,2} \\
J\dot{y}^{1}_{,2} &= \bar{x}_{3,2}\,\bar{x}_{1,3} - \bar{x}_{3,3}\,\bar{x}_{1,2} \\
J\dot{y}^{1}_{,3} &= \bar{x}_{1,2}\,\bar{x}_{2,3} - \bar{x}_{1,3}\,\bar{x}_{2,2} \\
J\dot{y}^{2}_{,1} &= \bar{x}_{2,3}\,\bar{x}_{3,1} - \bar{x}_{2,1}\,\bar{x}_{3,3} \\
J\dot{y}^{2}_{,2} &= \bar{x}_{3,3}\,\bar{x}_{1,1} - \bar{x}_{3,1}\,\bar{x}_{1,3} \\
J\dot{y}^{2}_{,3} &= \bar{x}_{1,3}\,\bar{x}_{2,1} - \bar{x}_{1,1}\,\bar{x}_{2,3} \\
J\dot{y}^{3}_{,1} &= \bar{x}_{2,1}\,\bar{x}_{3,2} - \bar{x}_{2,2}\,\bar{x}_{3,1} \\
J\dot{y}^{3}_{,2} &= \bar{x}_{3,1}\,\bar{x}_{1,2} - \bar{x}_{3,2}\,\bar{x}_{1,1} \\
J\dot{y}^{3}_{,3} &= \bar{x}_{1,1}\,\bar{x}_{2,2} - \bar{x}_{1,2}\,\bar{x}_{2,1}
\end{aligned} \tag{39}$$

and

$$J\dot{y}^{j}_{,t} = -\sum_{k=1}^{3} J\dot{y}^{j}_{,k}\,\frac{\partial \bar{x}_k}{\partial \tau} \tag{40}$$

Grid Transformation

The flow over a nozzle boattail configuration entails regions of large shear near the surface of the boattail and in the shear layer coming off the trailing edge as seen in Fig. 2, curve h-g. We must, therefore, allow for mesh clustering in both the streamwise and radial direction at the body's surface and in the interior of the flow field. In addition, the boattail surface should correspond to a coordinate line in order to enable one to easily impose the appropriate surface boundary conditions.

The methods employed in the construction of the coordinate system are based on generalizations of the Roberts type transformation, Ref. (48). Several different analytic forms were used to cluster the grid points.

In the computational space the grid spacing is uniform and for simplicity set to 1, i.e. $\Delta x = 1.0$. In the present problem the constraints of the grid transformation are chosen so that the boundaries of the computational domain fall on grid points. In addition, the boundary of the boattail surface is chosen to lie on grid point number m, for instance. The choice of the grid spacing between points m + 1 and m is based on physical considerations such as the requirement that the first point above the surface should lie within the sublayer of the turbulent boundary layer. An analogous procedure is used to distribute the grid in the streamwise direction, but in this case the base is fixed at a desired grid point.

This type of procedure gives the desired degree of flexibility for the problems under consideration. Furthermore, since the grid distribution in the streamwise and radial directions are independent, the grid will in general be nonorthogonal. This feature, rather than being an impedement turns out to be beneficial in that we do not overly constrain the problem to conform to say an orthogonality condition, which would necessarily distort the boattail base (cf. Ref. 22) when using a body fitted coordinate system. By allowing for a nonorthogonal grid the shape of the boattail can be preserved. Obviously, the sharp corner at the intersection of the base and shoulder introduces a singular point into the calcultion which must be treated appropriately. In the following section, this matter is taken up and discussed.

Treatment of the Corner Points

Corner points such as point h of Fig. 2 where the boattail shoulder intersects the base present special problems to finite difference schemes and this flow region has been the subject of several recent investigations. An overview of the

problem is given by Roache Ref. (49) who points out that this region may be subject to large truncation error. In addition, as discussed by Roache the question of whether the potentially large truncation error is confined to the immediate region of the corner or whether it has a much larger global effect is still unresolved.

Several types of methods have been proposed for treating this region. A common practice is to eliminate the corner by rounding it, and thus avoid the problem completely. But, this method changes the geometry under consideration. Alternatively at the corner a local analysis can be undertaken Refs. (50-51). As discussed by Fox (Ref. 50), Fox and Sankar (Ref. 51) represent the singular behavior of the flow by using special equations based upon a series expansion in the immediate vicinity of a wall singularity (such as the wall corner point). A second approach which also isolates this area has been developed by Ladeveze and Peyret (Ref. 52) who match an asymptotic solution of the flow in the vicinity of the corner with a finite difference solution of the Navier-Stokes equations elsewhere. But this approach leads to a more complicated calculation, since the embedded local analysis must be matched to the main flow field computation. The inherent errors such as interpolating onto the "large" domain could offset the gains of using an embedded domain analysis technique. Furthermore, the two domain algorithm assumes that the grid is sufficiently fine in the corner region. This may lead to undue strain on the grid spacing in the "large" domain or additional grid points must be included, leading to increased run times.

As a compromise between these two approaches the "double valued" technique was chosen. As discussed by Roache (Ref. 49) the method to be utilized is based upon discontinuous values of dependent variables at the corner point. As shown in Fig. 2, the corner point, h, can be approached from either a horizontal or vertical direction. If the required boundary condition is a derivative condition, the value at the corner will depend upon whether the derivative is taken in the horizontal or vertical direction. The situation is resolved by taking h as a double-valued point; i.e., a second grid point is located a minute distance from the corner and dependent variables may be discontinuous between the two points representing the corner. One of the points would be used in evaluating derivatives in the horizontal direction and the other point would be used in evaluating derivatives in the vertical direction.

In this technique the corner remains sharp, maintaining the original geometry, but the singular point is allowed to exist in that the values of the pressure and

density are permitted to vary depending on the coordinate direction from which the corner is approached. This type of approach fits in naturally with the ADI procedure since the double values are associated with the appropriate implicit direction. It is important to note that only quantities whose functional values are not known at the corner assume a double value, i.e. non function boundary conditions are applied there. Since the no-slip condition is applied at the wall, the velocity components are single valued and are set equal to zero. However, the pressure and density become double valued at the corner since the boundary condition used to evaluate these variables involve derivatives. If a gradient condition were used for the wall enthalpy (heat transfer rate prescribed) then the enthalpy would also be double valued at the corner. In our case, the wall enthalpy is prescribed so that a single value of the enthalpy was employed.

SOLUTION PROCEDURE

The computer code is based upon an axisymmetric version of the highly efficient consistently split, linearized block-implicit solution procedure (MINT) for the compressible Navier-Stokes equations developed by Briley and McDonald (Refs. 53, 32, 33), and subsequently extended to multi-component, chemically reacting, turbulent flows by Gibeling, McDonald and Briley (Ref. 34). This procedure solves the Navier-Stokes equations written in primitive variables; in the MINT procedure, the governing equations are replaced by either a Crank-Nicholson or a backward time difference approximation. Terms involving nonlinearities at the implicit time level are linearized by Taylor series expansion about the known time level, and spatial difference approximations are introduced. The result is a system of two-dimensional coupled linear difference equations for the dependent variables at tht unknown or implicit time level. These equations are solved by the Douglas-Gunn (Ref. 35) procedure for generating ADI schemes as perturbations to fundamental implicit difference schemes. This technique leads to systems of one-dimensional coupled linear difference equations which are solved by standard block-elimination methods, with no iteration required to compute the solution for a given time step. An artificial dissipation term based upon either a cell Reynolds number criterion or the rate of change of the dependent variable may be introduced selectively into the scheme to allow calculations to be performed at high local values of the cell Reynolds number.

The use of an implicit solution procedure requires that equation coupling and linarization be considered. Both of these topics are reviewed in detail by McDonald and Briley (Ref. 54) and Briley and McDonald (Ref. 32). There it is shown that for a given spatial grid the errors arising from time linearization of the nonlinear terms at the unknown time level should be no greater than the discretization errors. Weinberg and McDonald in Ref. (55) also demonstrated this result for a model problem. Furthermore, reduction of the time step is the preferred way of reducing the linearization error since transient accuracy is thereby improved. Linearization by Taylor series expansion in time about the known time level introduces errors no greater than those due to the differencing (Refs. 41 and 18), and this approach has been employed here. The formal linearization process results in a system of coupled equations in order to retain the requisite order of temporal accuracy. The system of coupled equations at the implicit time level is solved efficiently using a standard block elimination matrix inversion scheme. In the present problem, the strong coupling effects among the governing equations dictate the use of the block

coupled equation approach. However, weakly coupled equations could be solved in a decoupled manner in order to reduce computer time and storage requirements. A description of the linearization technique and the ADI procedure is given in Appendix B.

Initial and Boundary Conditions

The solution procedure requires that initial and boundary conditions be specified. Although the time asymptotic solution of the Navier-Stokes equations is independent of initial conditions, a prudent choice of initial conditions could hasten convergence. The initial conditions that were chosen for the problems of interest essentially involved the translation of the profiles of the dependent variables at the upstream boundary throughout the computational domain with the constraint that the profiles satisfy the boundary conditions at the surface of the body.

The choice of boundary conditions is not as arbitrary, and depends on the physics of the problem. Since the external flow is supersonic at the inflow boundary, profiles of the dependent variables are specified in accordance with an inviscid characteristic analysis. At the surface of the body no-slip and constant wall enthalpy boundary conditions are used. The latter condition was used due to its simplicity, and could have easily been replaced by a derivative condition (heat transfer rate) on option. An additional condition is needed for the remaining variable, the density. Both the normal momentum equation evaluated at the solid boundary and the normal derivative of pressure have been used successfully. Along the axis of the boattail, symmetry boundary conditions are employed while at the downstream outflow boundary second derivative extrapolation conditions are applied. These extraneous conditions are used in lieu of special differencing to eliminate the exterior points. In view of the reasonable nature of the physical approximations involved this is found to be both convenient and realistic, and we had no difficulty in applying them. However, at the top boundary, where waves generated in the interaction process in the vicinity of the boattail must exit the computational domain special attention must be given to the appropriate choice of boundary conditions. In order to prevent these waves from reflecting from the top boundary back into the computational domain and perhaps polluting the solution, a Mach wave extrapolation condition was developed. A description of this boundary condition is given in some detail in the next section.

Mach Wave Extrapolation

Consider a nonorthogonal coordinate system (y^1, y^2, y^3) and a Cartesian system (x^1, x^2, x^3) with Cartesian velocity components (u^1, u^2, u^3).

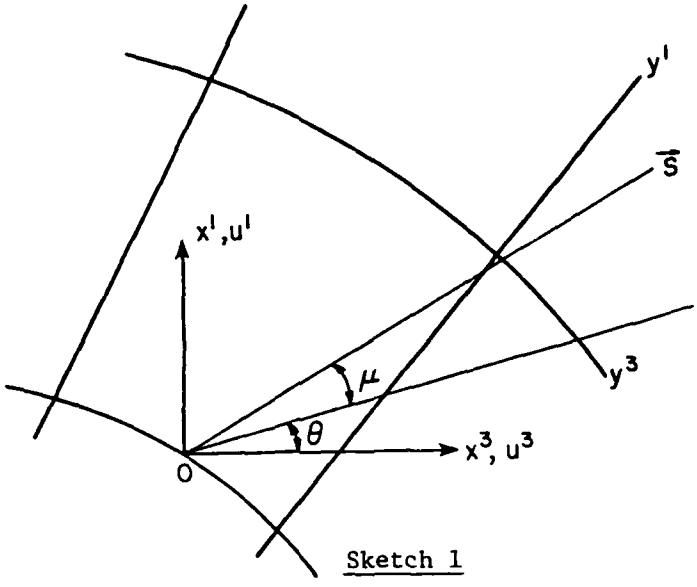

Sketch 1

Through point 0 we may draw the streamline and Mach wave inclined at an angle μ with respect to the streamline. The streamline is at an angle θ measured with respect to the Cartesian coordinate x^3.

Now

$$\mu_0 = \sin^{-1}\left(\frac{1}{\mu_0}\right) \tag{41a}$$

and

$$\theta_0 = \tan^{-1}\left(\frac{u^3}{u^1}\right)_0 \tag{41b}$$

which leads to a total included angle with respect to x^3 of

$$\psi = \theta_0 + \mu_0 \tag{42}$$

The mach wave passing through point 0 can be represented as the vector $\vec{s}$

$$\vec{s} = \sin\psi\,\hat{i}_1 + \cos\psi\,\hat{i}_3 \tag{43}$$

where $\hat{\imath}_1$ and $\hat{\imath}_3$ are unit vectors in the x^1 and x^3 directions respectively. For any scalar function Φ the gradient is given by

$$\nabla\Phi = \Phi_{,1}\hat{i}_1 + \Phi_{,3}\hat{i}_3 \tag{44}$$

The component of $\nabla\Phi$ in the $\vec{s}$ direction is obtained by the dot product

$$\vec{s}\cdot\nabla\Phi = \sin\psi\,\Phi_{,1} + \cos\psi\,\Phi_{,3} \tag{45}$$

so that the mach wave extrapolation condition, i.e. Φ along a mach wave is constant, becomes

$$\sin\psi\Phi_{,1} + \cos\psi\Phi_{,3} = 0 \tag{46}$$

Relating the Cartesian coordinates (x^i) to the physical coordinates (y^i) we obtain

$$\begin{aligned}\Phi_{,1} &= \frac{\partial\Phi}{\partial y^1}\frac{\partial y^1}{\partial x^1} + \frac{\partial\Phi}{\partial y^3}\frac{\partial y^3}{\partial x^1}\\ \Phi_{,3} &= \frac{\partial\Phi}{\partial y^1}\frac{\partial y^1}{\partial x^3} + \frac{\partial\Phi}{\partial y^3}\frac{\partial y^3}{\partial x^3}\end{aligned} \tag{47}$$

Substituting Eq. (47) into equation (46) we obtain

$$\frac{\partial\Phi}{\partial y^1} + \sigma\,\frac{\partial\Phi}{\partial y^3} = 0 \tag{48}$$

where

$$\sigma = \frac{\dfrac{\partial y^3}{\partial x^1} + \cot\psi\,\dfrac{\partial y^3}{\partial x^3}}{\dfrac{\partial y^1}{\partial x^1} + \cot\psi\,\dfrac{\partial y^1}{\partial x^3}} = \frac{N}{D} \tag{49}$$

Now σ is a nonlinear function of the velocity components u^1, u^3 and h the enthalphy via the evaluation of the angle ψ. We must, therefore, linearize this term about the known time level n.

$$\sigma^{n+1} = \sigma^n + \left(\frac{\partial \sigma}{\partial u^1}\right)^n \Delta u^1 + \left(\frac{\partial \sigma}{\partial u^3}\right)^n \Delta u^3 + \left(\frac{\partial \sigma}{\partial h}\right)^n \Delta h \tag{50}$$

where

$$\frac{\partial \sigma}{\partial u^1} = - \frac{(\csc^2 \psi)^n}{D^n} \left[\frac{\partial y^3}{\partial x^3} - \sigma^n \frac{\partial y^1}{\partial x^3} \right] \left(\frac{\partial \psi}{\partial u^1} \right)^n = - \Omega^n \left(\frac{\partial \psi}{\partial u^1} \right)^n$$

and similarly

$$\frac{\partial \sigma}{\partial u^3} = - \Omega^n \left(\frac{\partial \psi}{\partial u^3} \right)^n$$

$$\frac{\partial \sigma}{\partial h} = - \Omega^n \left(\frac{\partial \psi}{\partial h} \right)^n$$

Hence

$$\sigma^{n+1} = \sigma^n - \Omega^n \left[\left(\frac{\partial \psi}{\partial u^1} \right)^n \Delta u^1 + \left(\frac{\partial \psi}{\partial u^3} \right)^n \Delta u^3 + \left(\frac{\partial \psi}{\partial h} \right)^n \Delta h \right] \tag{51}$$

The Mach wave extrapolation boundary condition is employed on the first sweep of the ADI procedure (in the x^1 direction), at the * level. This condition reduces to the following equation

$$\frac{\partial \Phi}{\partial y^1} + \sigma \frac{\partial \Phi}{\partial y^3} = 0$$

or

$$\frac{\partial \Delta \Phi^*}{\partial y^1} + \sigma^{n+1} \left(\frac{\partial \phi}{\partial y^3} \right)^n = - \left(\frac{\partial \phi}{\partial y^1} \right)^n \tag{52}$$

using the linearized form of σ^{n+1} we obtain

$$\frac{\partial \Delta\phi^*}{\partial y^1} - \Omega^n\left[\left(\frac{\partial \psi}{\partial u^1}\right)^n \Delta u^1 + \left(\frac{\partial \psi}{\partial u^3}\right)^n \Delta u^3 + \left(\frac{\partial \psi}{\partial h}\right)^n \Delta h\right] \tag{53}$$

$$= -\left[\sigma^n\left(\frac{\partial \phi}{\partial y^3}\right)^n + \left(\frac{\partial \phi}{\partial y^1}\right)^n\right]$$

where ϕ is either u^1, u^3 or h.

One could lag the Mach angle (evaluate it at the n^{th} time level) by setting $\Omega^n = 0$. For our case this simplification was used since we were interested only in a steady solution, and the flow near the outer boundary was well behaved.

DISCUSSION OF RESULTS

Several different aft end flow fields are discussed. In order to verify the code, i.e. L-shaped domain and corner point treatment as well as the adaptive grid capability the laminar supersonic two-dimensional right angle backstep was considered. Turbulence modeling effects were investigated in the supersonic axisymmetric test case of Badranarayan (Ref. 57). In both these cases the expected qualitative behavior was obtained. However, the results will not be discussed in any great detail except where relevant to the studies they were specifically designed to address. The cases that are considered in detail are the flow over the AGARD 10° nozzle boattail at $M_\infty = 1.5$ with and without jet exhaust. These cases correspond to the experiments of Galigher, et al (Ref. 5). In addition, the two-dimensional supersonic flow over a rearward facing step and the subsequent reattachment of the free shear layer on a 20° inclined ramp will also be described. This case, which corresponds to the data of Settles, et al (Ref. 58) was submitted by SRA to the 1981 AFOSR -HTTM- Stanford Conference on Complex Turbulent Flows.

Mesh Movement - Adaptive Grid

In the solution of problems where regions of large gradients occur, lack of mesh resolution can lead to oscillations, cell Reynolds problems or give misleading results. Whenever these regions can be isolated and identified then standard mesh refinement techniques such as those discussed in this report can be implemented. However, in many cases these regions either cannot be identified a priori or they change in time as the solution procedure progresses. There is, therefore, great interest in being able to adapt the grid to the particular problem. Two aspects of the grid adaptor procedure must be considered. The first is the actual process of moving the grid and the second, the far more difficult, is the choice of criteria by which the grid moves. The latter point becomes even more difficult if we wish to automatically adapt the grid by monitoring particular functions or derivatives, since we do not wish to mislead the geometry into clustering grid points in inappropriate regions or by moving it too rapidly.

The first problem of actual grid movement is accomplished by using the time-dependent geometry form of Navier-Stokes equations that has been applied by Gibeling and McDonald Ref. (59) to interior ballistics. The metric data is cast into a form that it is a function of time. Hence, the governing equations contain terms that account for geometry movement (they appear as convection terms). This

procedure eliminates any need to interpolate data from one grid onto another across a time step. An alternate approach would entail interpolating onto a new grid at the end of a time step, and then marching the solution from there. The main advantage of this procedure is that it simplifies the evaluation of geometric germs since it is now independent of time. However, it has the disadvantage, as previously mentioned, of requiring the interpolation of the entire flow field onto the new grid whenever the grid is moved. Since the time dependent geometry option allows for geometries that can change in time, i.e. expanding domains, the additional generality influenced the choice of method. However, the alternate approach could be useful for certain applications and deserves further consideration.

The second problem of choosing the criteria by which the mesh is modified in time is now considered. Our aim is to redistribute the number of grid points so that they are concentrated in the region of the free shear layer. In order to locate the shear layer, the region of large gradients, an optimization routine developed by Levy (Ref. 60) was adapted for the MINT code. We assume that the shear layer begins at the corner point (cf. Fig. 3) and can be represented by an analytic function. In this case, it was chosen to be a cosine function, i.e.

$$x = x_0 + A\,(1 - \cos\lambda(z - z_0)) \qquad \lambda(z - z_0) \le \Pi \tag{54}$$

$$x = x_0 + 2A \qquad \lambda(z - z_0) > \Pi$$

where x_0 and z_0 are the coordinates of the corner and the two underdetermined coefficients A and λ, the amplitude and wave length respectively are functions of time. The cosine function was chosen due to its simplicity, but any other convenient function could have been used. In the vicinity of the shear layer the flow field is sampled for the magnitude of the first derivative of the dependent variables. The data is then filtered and an "optimum" curve is derived (e.g. A and λ are chosen) that best fits the data and has the functional form given by equation (54).

Assume for the moment that the original mesh was orthogonal and that a Robert's type transformation was employed that was centered about the line $x = x_0$, where x_0 is the location of the corner (cf. Fig. 3). The shear layer will in general depart from the original horizontal line $x = x_0$. Since we wish to cluster points in the vicinity of the shear line, we center the grid transformation about this new computed curve. Note that the resulting grid will no longer be orthogonal in the region of the shear layer. Both levels of geometry, the original orthogonal grid at the n^{th} time level and the new nonorthogonal grid at the $(n + 1)$st time level are employed to advance the solution one step in time. At this point, the data can be sampled again

to determine a new location of the shear layer. The process is repeated at some predetermined frequency (in time) or until the shear layer position does not change within some preset tolerance.

This adaptive grid option was examined for the laminar two-dimensional flow over a back step at a Mach number of $M_\infty = 3$ and Reynolds number based on step height of $Re_h = 400$. A velocity vector plot of the flow field is shown in Fig. 4. Two tests were conducted. In the first, the grid was forced to move through half a cycle which corresponds to the maximum deviation from the initial state of a horizontal line. The purpose of this test was to verify that the solution is well behaved during the mesh movement, and to determine how sensitive the solution was to the mesh clustering about the shear layer. Figure 5 shows the velocity profiles at two locations downstream of the base, in the recirculation zone and in the wake before and after the mesh movement. The results compare very well with each other indicating that the method does not introduce errors due to grid movement and that in the case of interest the solution is not very sensitive to the location of the shear layer. It is expected, however, that for other cases in particular for turbulent flows greater mesh sensitivity would be encountered. The second test case was designed to allow the grid to move under the control of the optimization curve fit procedure described previously. In Fig. 6 the velocity profiles in the wake and recirculation zone are compared again prior to and after mesh movement. The results compare well with one another. In the case considered, the original orthogonal grid had adequate resolution in the shear layer and, therefore, the use of an adaptive grid did not have a substantial effect on the results. In other problems being considered at SRA this is not the case. For instance in the normal shock calculations (ARO Contract DAAG29-80-C-082) the adaptive grid procedure aided in stabilizing the moving shock and resolving the details of its structure.

Although for the cases considered in this report (e.g. boattail geometry) the adaptive grid option would have been useful, we did not proceed with its implementation at the present time. A primary reason was that the hyperbolic function grid transformations that were employed initially in order to cluster points within the shear layer did not have the desired grid control under mesh movement. This is in part a consequence of the physics of the problem which leads to a "shear layer curve" that is a function of x and z as compared to the normal shock which is primarily a function of z alone. For the normal shock case adequate grid control was obtained. Recently, new grid transformations have been developed that alleviate this problem and allows for better grid control. They have not as yet been used in adaptive grid calculations.

Nozzle Boattail

Experimental data is very limited for the cases of interest; the supersonic axisymmetric turbulent flow over a boattail geometry with and without jet exhaust. Either the geometry is inappropriate, i.e. 2-D versus axisymmetric, or the flow is subsonic or insufficient data is given. The case chosen with which to compare our calculation was that of Galigher, et al (Ref. 5). This case has two main shortcomings, the data is incomplete, there are only pressure measurements for the shoulder and no measurments at all in the interaction zone downstream of the base, and there are three dimensionality effects due to the model supports. Although, at the outset of our calculation these shortcomings were evident, it was felt that the data for the pressure signature on the shoulder should be reliable, and of sufficient interest to warrant their consideration. Furthermore, the jet on case was computed by Mikhall, et al (Ref. 22), and this seemed to afford us a means of comparing our calculations with other results. Unfortunately, the lack of data was a far greater detriment than expected. Since our results indicate that the pressure signature on the shoulder is sensitive to the turbulence model, additional data on the shoulder, i.e. velocity profiles as well as in the jet and wake could have been useful in selecting the appropriate length scales. Although the calculations showed less sensitivity to upstream turbulent boundary layer parameters, additional data by the experimentalists could have been of value. Originally, we had intended to compare our calculations with those of Mikhail, et al (Ref. 22). However, due to significant differences in the geometry adopted and substantial differences in turbulence modeling as compared to that adopted here, it was decided that a comparison with the calculation of Mikhail could be misleading and this is deferred until some of the questions that are raised later in this report can be resolved.

In this section we describe the construction of the coordinate system for the boattail geometry, the boundary conditions and turbulence model employed and the results of our calculations for the jet on and jet off cases.

Figure 7 shows the AGARD 10° nozzle boattail configuration with the coordinate information given in tabular form. In order to simplify subsequent computations, the geometric data was represented by a least square cubic curve fit given as

$$r = 4.93 - .022948x - .00302x^2 - .0003747x^3 \qquad (55)$$

The maximum error between the analytic representation and the actual boattail shape was less than 1.5%.

The computational domain is shown in Fig. 8, and includes moving counter-clockwise the upstream boundary, boattail shoulder, boattail base and jet exit, symmetry line, downstream boundary and the outer boundary. Note that the region external to the boattail body is L-shaped. The upstream boundary was chosen at 5 baseheights upstream of the base, the downstream boundary at 8 base heights downstream of the base and the outer boundary at 4 base heights above the symmetry line.

The first task was to construct a coordinate system with a sufficient distribution of grid points to adequately resolve the flow field within the computational domain, while satisfying the constraints that all boundaries must lie on coordinate lines and the base shoulder interaction remain sharp. As discussed in an earlier section, this leads to a nonorthogonal grid distribution. In the following, the grid construction is outlined.

Consider the rectangle enclosing the boattail. It includes as sides the upstream and downstream boundaries and the outer boundary and symmetry lines. The z = constant lines (vertical lines) are constructed first. Since these lines do not vary with x a single distribution is required which assures that the upstream and downstream boundaries lie on grid points and that the base, which is in the interior also lies on a grid point. We employ an analytical transformation which satisfies the above conditions and allows for grid spacing control to the requisite degree of resolution in the vicinity of the base. Refer to Fig. 9 for the z distribution. In the case we considered, there were 41 grid points in the z direction with the base falling on the 20th grid point.

Having obtained the z distribution we are in a position to construct the x distribution. The constraints for this portion of the grid generation process are that the outer and symmetry boundaries lie on grid points. In addition, the boat-tail surface must also be a coordinate line. Since the boattail surface terminates at the base, we must analytically extend it in order that the metric data be continuous at the corner point. This was accomplished by passing a second order polynomial through the corner point, which matched the slope of the boattail at the corner and terminated at some location downstream of the base with a zero slope. For each z location, the upper boundary, the boattail surface and its extension and the symmetry line were required to lie on grid lines with the additional constraint that the grid spacing near the boattail surface be chosen to adequately resolve the turbulent sublayer. The analytic transformation used in

obtaining the z distribution was also used here and obtained the grid lines shown in Fig. 9. Note that in contrast to the z distribution which was not a function of x and was obtained in one pass, the x distribution was repeated at every z station. This is a direct consequence of the nonorthogonality of the grid, i.e. the x coordinate lines are functions of z. In the case under consideration 41 grid points were used in the x direction with the boattail surface lying on the 20th grid point. Since the points within the nozzle boattail do not lie within the computational domain, a total of 1320 grid points including boundaries were used for the computation. This is a rather meager number of grid points, and large stretches had to be used in order to satisfy the constraints that were placed on the transformation. More grid points could have eased the severity of the stretches while allowing better resolution. Whether there was adequate resolution in the interaction zone is still open to question. The jet on results indicate that immediately upstream of the base there was insufficient resolution. This question will be addressed in greater detail below.

In order to solve the Navier-Stokes equtions, appropriate boundary conditions must be specified. These are given below.

1. Upstream inflow boundary

   Profiles specified for u, w, h, ρ

2. Boattail surface and base

   $u = w = 0$

   $T = Tw$

   $\frac{\partial P}{\partial n} = 0$

3. Symmetry line

   $u = 0$

   $\frac{\partial w}{\partial n} = \frac{\partial h}{\partial n} = \frac{\partial \rho}{\partial n} = 0$

4. Downstream outflow boundary

   $$\frac{\partial^2 u}{\partial z^2} = \frac{\partial^2 w}{\partial z^2} = \frac{\partial^2 h}{\partial z^2} = \frac{\partial^2 \rho}{\partial z^2} = 0$$

5. Top outflow boundary

   Mach wave extrapolation for u, w, h, ρ

6. Jet at base

   $u = 0$

   w, h, ρ or P profiles specified

The freestream conditions for the boattail jet off condition are

$$M_\infty = 1.5 \qquad \text{and} \qquad Re_\infty = 2.5 * 10^6/\text{ft.}$$

The wall temperature was taken as $T_w = 580°R$. In order to obtain upstream turbulent profiles, the boundary layer thickness is needed. A value of $\delta = 1.12$ inches was chosen which corresponds to the estimate of Mikhail, et al (Ref. 22). Insufficient information is given in the experiment to obtain a precise value. A better approximation for the upstream profiles and δ could be obtained by exercising a marching procedure, e.g. the PEPSI-S Code (Ref. 61) and marching from the nose of the one cylinder until the upstream boundary of the Navier-Stokes computational domain. Numerical experiments indicated that decreasing δ did not have an appreciable effect on the pressure signature on the shoulder.

Employing the procedure of Maise and McDonald (Ref. 62) the appropriate constants for the Coles law profile can be obtained, and streamwise velocity profile computed. Assuming H_o = constant, u = 0, and that the pressure is constant across the boundary layer and equal to the free stream value, the density and enthalpy profiles can be obtained. Since these profiles are not precisely consistent with the interior solutions, a procedure was implemented in order to eliminate their effect on the Navier-Stokes solution. A preliminary calculation was performed, beginning upstream of the Navier-Stokes region, at z/h = -8 and terminating at z/h = -3. This computational domain starts in uniform flow and has no knowledge of the base and hence will not be influenced by upstream effects. The Navier-Stokes equations are solved within this domain, and the profiles that are obtained at z/h = -5 then become the upstream boundary conditions for the base region domain. The pressure coefficient obtained for this calculation is presented in Fig. 10. Also, on this figure are the c_p curves for the jet on condition. Note the three dimensionality of the experiment in the variation of the c_p curves for the upper and lower surfaces. The computed c_p curve which lies between the two experimental data curves is in fairly good agreement with the data.

A turbulence model must now be specified in order to obtain closure. An algebraic mixing length model, the one-equation k-ℓ model and the two-equation k-ε model were experimented with for a number of test cases. In our calculations of the supersonic axisymmetric backstep problem of Badranarynan (Ref. 57), a comparison of the mixing length and k-ℓ models was made. Both models are dependent on evaluating an appropriate length scale. On the surface of the body, this is relatively easy. However, in the wake it is much more difficult since we must detect the "edge" of the shear layer which is not well defined. However, the results obtained by both methods in the wake of the body were very close to one another.

During the calculation of the Stanford test case (see following section) the two-equation k-ε model was exercized. Difficulties were encountered immediately downstream of the corner in the recirculation zone. At least some of these difficulties were traced to the low Reynolds number correction terms that were devised to be used near solid boundaries, which apparently give rise to non-physical behavior in the free shear layer. In view of the lack of confidence in the k-ε model with no-slip boundary conditions and the absence of any substantial improvements in using the computationally more expensive k-ℓ model, the algebraic mixing length model was used to obtain the reported results.

Figures 11 - 16 show computer plots of the results of the calculation. In Fig. 11 the Mach number contours for the entire computational domain are presented. The interaction of the expansion wave on the shoulder with the separation compression wave is evident. Furthermore, the closing of the Mach number contours incidate the presence and extent of the recirculation zone. A blown up view of the coordinate system in the vicinity of the base is presented in Fig. 12. Several streamwise coordinate lines near the shoulder of the shoulder of the boattail have been eliminated for clarity. The pressure contours in this region are shown in Fig. 13. Note that the pressure minimum is in the center of the recirculation vortex and that the flow recompresses downstream of this location in the near wake. Further downstream (not shown in this figure) in the far wake, the flow reexpands. The next two figures 14 and 15 show the velocity vector plot for the full domain and the near wake region respectively. The turning of the shear layer and the resulting closed recirculation zone is clearly seen. These results are in keeping with the expected qualitative behavior.

As mentioned earlier, the sole data presented in Ref. 5 is for the pressure coefficient, c_p, on the shoulder of the boattail. In Fig. 16 we present a comparison of our calculations with the data of Ref. 5. From 1.5 to 8 base heights upstream of the base, the data for the upper and lower surfaces are shown with the spread in c_p values being indicative of the three dimensionality of the flow. For the section of the boattail in the vicinity of the corner only the top surface data is shown since we did not have available the bottom surface data. In the region from 3 to 5 base heights upstream the computed c_p curve is indistinguishable from the curve presented in Fig. 10 which was used to obtain the upstream boundary conditions and confirms that the location of the upstream boundary placement is not influenced by the interaction process.

As compared to the experimental data, the computations show a pressure rise that is delayed and thus leads to a smaller region of upstream influence. Although the pressure rise has the same slope as the data, there is no plateau or leveling out of the pressure as the corner is approached.

Several factors could have contributed to the quantitative lack of agreement. First is the turbulence modeling in the wake and on the shoulder. The turbulence model employed was an algebraic mixing length model. The mixing length on the shoulder was computed by Eq. (27). In the free shear layer and wake the mixing length was nominally computed from a linear expression relating ℓ_∞ at the corner and ℓ_∞ at some location downstream in the wake. The value of ℓ_∞ at the corner was the value obtained at the point of minimum pressure on the boattail shoulder and which was frozen at that value over the remainder of the boattail surface. In order to assess the effect of the length scale in the wake region on the boattail corner pressure, the value of ℓ_∞ was varied. This is shown in Fig. 17. As Z* is diminished, the effective ℓ_∞ in the recirculation is increased resulting in a greater turbulent viscosity and, hence, a lower corner pressure. The c_p results presented in Fig. 16 are for case 4.

The effect of the ℓ_∞ distribution on the boattail surface was not evaluated in such detail, but it would appear from our computations that it has a less significant effect than the ℓ_∞ distribution in the wake. However, the inherent assumptions of the mixing length, i.e. the turbulent viscosity is proportioned to the velocity gradients may be suspect in the separated region on the boattail. Further detailed investigation of the one and two-equation turbulence models would be of value in resolving this issue.

It must also be pointed out that the jet off computation did not correspond precisely with the actual experiment. Apparently, the jet off experiment was run with the nozzle open. This would allow fluid to enter the nozzle and thus give rise to a recirculation zone that was different than one that would exist if nozzle plane was a solid surface. The flow structure in the vicinity of the base would necessarily have an effect on the pressure at the corner.

To calculate the flow field with the nozzle open would require that the computational domain include a region inside the nozzle upstream of the exit plane. Although the computer code is designed to handle such geometries at this stage of the model development it was felt that the added complexity was not warranted. Thus, in the present computations a solid wall on the nozzle exit plane was assumed. In comparing the computations with data, it would appear that assuming a solid wall could have a significant effect on the boattail pressure signature. It is recommended that in any study aimed at resolving the discrepencies in the c_p

distribution additional effort should include expanding the computational domain into the interior of the nozzle.

Jet On Case

The next case we considered was a nozzle boattail with jet exhaust at a nozzle pressure ratio (NPR) of $P_{jet}/P_{o_\infty} = 7.09$. P_{jet} is the jet static pressure and P_{o_∞} is the free stream stagnation pressure. The other pertinent data are:

$$T_{jet} = 450°R \qquad M_{jet} = 1.08$$

Nozzle exit radius R = 1.991 inches

Since the jet is supersonic, function data in the form of profiles of the dependent variables can be applied as boundary conditions. Note that the jet does not span the entire base area and this results in split boundary conditions on the base that changes abruptly at the jet/wall juncture. No computational problems were observed as a result of applying such boundary conditions.

The jet issuing from the nozzle is assumed to have a streamwise velocity distribution given by

$$\begin{aligned} W(r) &= W_j & 0 \le r \le R^* \\ W(r) &= W_j \left(\frac{R-r}{\delta}\right)^{1/7} & R^* < r \le R \end{aligned} \tag{56}$$

where W_j is the jet centerline velocity, $\delta = .1R$ and $R^* = .9R$, while the normal velocity is set to zero. In addition the stagnation temperature of the jet is assumed constant as is the static pressure. This model was used to obtain the appropriate density and static enthalpy profiles. The same grid distribution was used for both the jet off and jet on cases. At the base, the jet exit area encompassed grid points 1 - 11 while the solid wall was located on grid points 12 - 20.

The results of the calculations are shown in Figs. 18 - 22. In Fig. 18 the Mach number contours are presented for entire computational domain. The pattern is very different from the jet off case. With the jet on there is very little turning and in the near wake there is a rapid expansion. This is more clearly evident in Fig. 19 where the pressure contours are shown in the vicinity of the base. In Figs. 20 and 21 the velocity vector plots for the entire computational domain and for the near wake region are presented. The recirculation

zone on the shoulder, upstream of the corner, can be seen indicating the relatively large region of upstream influence. These results are in keeping with the expected physical behavior of the jet interaction.

The computed c_p distribution on the shoulder is shown in Fig. 22 where it is compared to the data in Ref. 5. The pressure rise in the vicinity of the base is somewhat delayed when compared to the data, and overshoots the experimental peak c_p. Also, near the corner oscillations in c_p are noted. The oscillations are believed grid dependent and could be eliminated by resolving the region near the corner with a finer grid. The reason for the overshoot and delay in the pressure rise is still unresolved, but as in the jet off case, it is believed that turbulence modeling plays a significant role.

Rearward Facing Step

The solution procedure described in the previous section is also used to compute the two-dimensional supersonic turbulent flow over a rearward facing step with shear layer reattachment on an inclined ramp. The numerical results that are compared with the data of Settles, et al (Ref. 57) were submitted by SRA, Inc. to the "1981 AFOSR -HTTM- Stanford Conference on Complex Turbulent Flows". The interesting feature of this problem is that the process of reattachment can be studied without complicating the upstream, incoming flow, with shock and expansion wave effects. These effects are present when we consider a simple back step flow. In that case the expansion wave eminating from the vicinity of the corner and the recompression shock influence the shear layer development and complicate the initial conditions of reattachment. By carefully adjusting the experiment Settles, et al (Ref. 58) were able to isolate the reattachment process by allowing the free shear layer to leave the back step parallel to the wall with no wave disturbance.

The experimental model and a schematic of the flow field is shown in Fig. 23 with the appropriate dimensions. The flow field contains two corners, the back step and the cavity ramp juncture. The former was kept sharp since the geometry at that location has a strong influence on the flow structure while the ramp cavity juncture was rounded with a small circular fillet. The rounding of the cavity ramp juncture is not expected to be an appreciable effect on the structure of the redeveloping flow. The construction of the geometry deserves special attention. Since the incoming flow is parallel to the upper surface of the back step, it is desirable to construct the x^3 coordinate lines parallel to this surface. Similarly, since

the outgoing flow will eventually align itself with the ramp, it is also desirable to construct the x^3 coordinate lines parallel to the ramp near the exit of the computational domain. Within the computational domain the x^3 coordinate lines must then vary smoothly between these two extremes. the x^1 coordinate lines by the same token should be orthogonal to the x^3 coordinate lines at the entrance and exit of the computational domain. However, within the computational domain the coordinates become nonorthogonal (cf. Figs. 24 and 25). The actual construction of the coordinate system is briefly described below.

Consider the computational domain (cf. Fig. 24) which is set off by the bold lines. Moving counterclockwise we start at the upstream boundary, and proceed over the back step surface, the base and the cavity floor. This is followed by a 20° inclined ramp, the exit plane that is perpendicular to the ramp and finally the outer boundary which begins parallel to the ramp and ends up parallel to the back step surface. Note that the cavity ramp juncture as well as the outer boundary are rounded with circular fillets so that the metric data in these locations would remain smooth. In order to construct the desired coordinate system, we focus on the trapezoid ABCD that encompasses the computational domain. First consider the coordinate lines which intersect the upper and lower boundaries. The constraints which are imposed are that the inlet AED, the exit BGC and the line containing the base all lie on coordinate lines. Furthermore, with the conditions that the grid spacing is prescribed these lines and that the line adjacent to the exit is orthogonal to the ramp we can construct the required grid distribution by employing a hyperbolic function transformation. This is accomplished by distributing points both along the top and bottom sides of the trapezoid (lines AB and CD) and connecting the corresponding points by straight lines (cf. figures 24 and 25).

In order to obtain the other family of coordinates we use the same approach as for the boattail and construct the curve EFG which has zero slope at the corner F and is parallel to the ramp at point G. Employing the procedure used in the construction of the streamwise cooridnate lines for the boattail geometry, the coordinate system shown in Fig. 25 is obtained.

The flow conditions for the problem are

$$M_\infty = 2.92$$

$$Re = 6.7 \times 10^7/\text{meter}$$

$$Tw = 265°k$$

The governing equations, continuity, two Cartesian momentum, energy and state are solved coupled, with the following boundary conditions:

1. Upstream inflow boundary

   Profiles specified for u, w, h, ρ

2. Backstep surface, base, cavity and ramp

   $u = w = 0$

   $T = Tw$

   $\frac{\partial \rho}{\partial n} = 0$

3. Downstream outflow boundary

   $$\frac{\partial^2 u}{\partial z^2} = \frac{\partial^2 w}{\partial z^2} = \frac{\partial^2 h}{\partial z^2} = \frac{\partial^2 \rho}{\partial z^2}$$

4. Top outflow boundary

   Mach wave extrapolation for u, w, h, ρ

The turbulence model used here was also an algebraic mixing length model with ℓ_∞ linearly increased in the wake until it reached a value of $\ell_\infty = .09\ \delta_a$ the average δ on the ramp which corresponds to $\ell_\infty = .039$.

It has been found necessary to add an artificial dissipation term in the numerical algorithm in order to suppress wiggles that could appear in regions of large cell Reynolds number. However, adding too much dissipation could smear out shock waves. In Ref. (63) it is shown that by appropriately dialing down the dissipation we can sharpen the shock waves. Such a method has been employed for the results presented here.

In Fig. (26) the pressure contours are shown. The pressure disturbance produced at the corner is inclined at the local Mach angle, while the compression wave that is generated in the reattachment process coalesces into a shock. The velocity vector plot presented in Fig. (27) confirms that the shear layer is parallel to the cavity wall. Furthermore, the recirculation zone contains three vortices. This is physically plausible since the ramp elongates the recirculation and causes a small vortex to be snipped off, and kinematic considerations require there to be an odd number of vortices.

Of major interest is a comparison of the velocity profiles in the shear layer and on the ramp. These results are shown in Figs. 28 and 29. There is fairly good agreement between the computations and the experiment. In particular the presence of the recompression shock on the ramp is evident in profile F.

The discrepancies that are noted are due in part to the mixing length turbulence model that was employed. Grid refinement on the ramp and moving the exit plane further downstream could also aid in obtaining better agreement.

CONCLUSIONS

In this report the development of a Navier-Stokes solution procedure that could be used to compute the aft end flow field over missile type bodies is presented. Special attention was given to handling the L-shaped domain that is encountered, the treatment of the sharp reentrant corner and the application of the appropriate boundary conditions.

An adaptive grid option was exercised for a model back step problem where the free shear layer was tracked and the grid distribution was automatically adjusted about this mean free shear layer curve. Calculations were performed for the supersonic turbulent flow over a 10° nozzle boattail configuration with and without jet exhaust. The qualitative physical behavior was obtained both on the shoulder and in the wake. Discrepancies in the shoulder c_p signature were traced at least in part to the turbulence modeling. For the jet off case, the assumption of a solid base rather than an "open nozzle exit" could account for some of the observed differences. For the jet on case greater grid resolution is required in the vicinity of the corner.

The calculation of the supersonic turbulent flow over a 2-D back step with shear layer reattachment on a 20° inclined ramp was also presented and the results were compared with experimental data. The flow field results showed qualitative physical behavior while the velocity profiles in the shear layer and on the inclined ramp compared well with data. The discrepancies that were observed can be traced again in part to turbulence modeling, grid resolution and placement of the downstream boundary.

Further evaluation of an appropriate turbulence model for the cases considered is crucial in obtaining more accurate results. Additional investigation of the effect of grid distribution and resolution is also warranted.

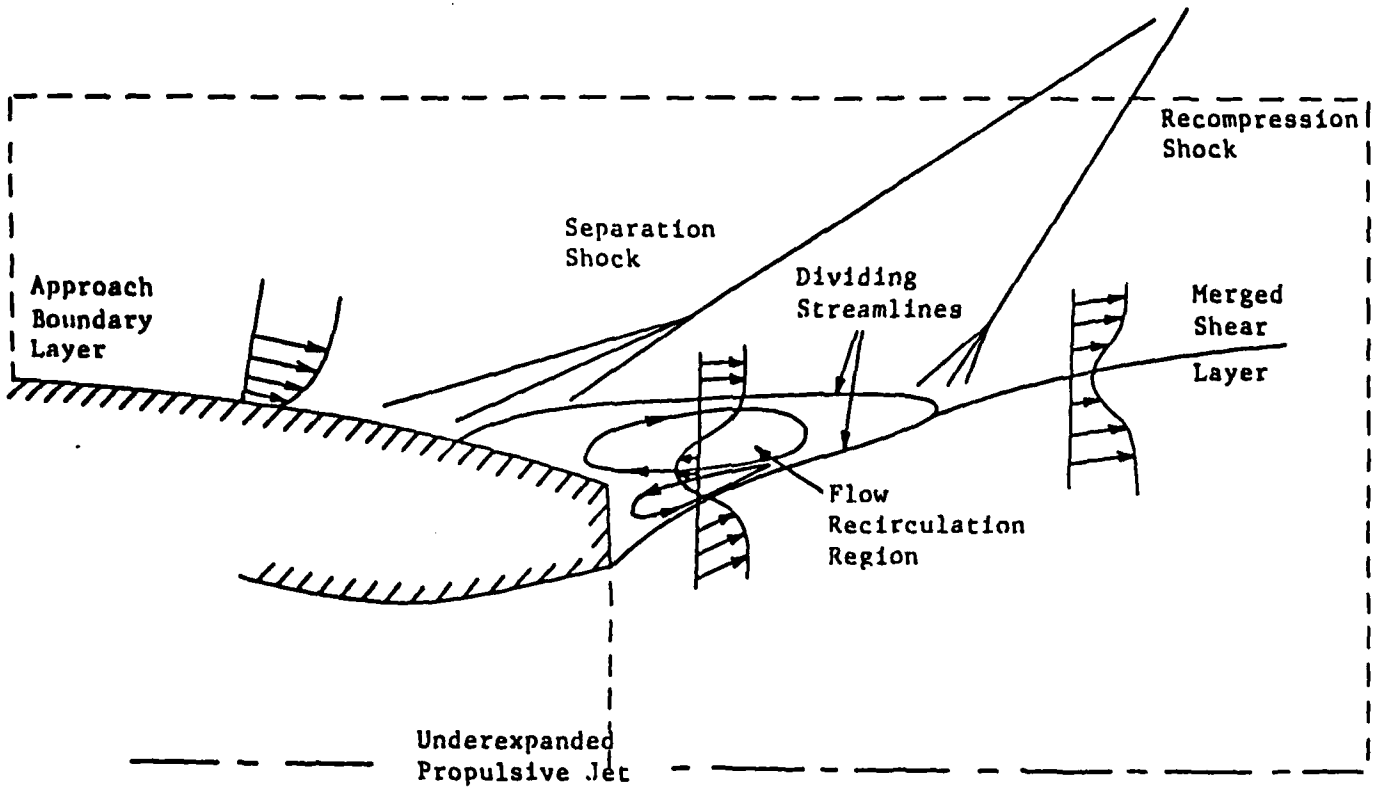

Figure 1 - Schematic of Plume Induced Separation.

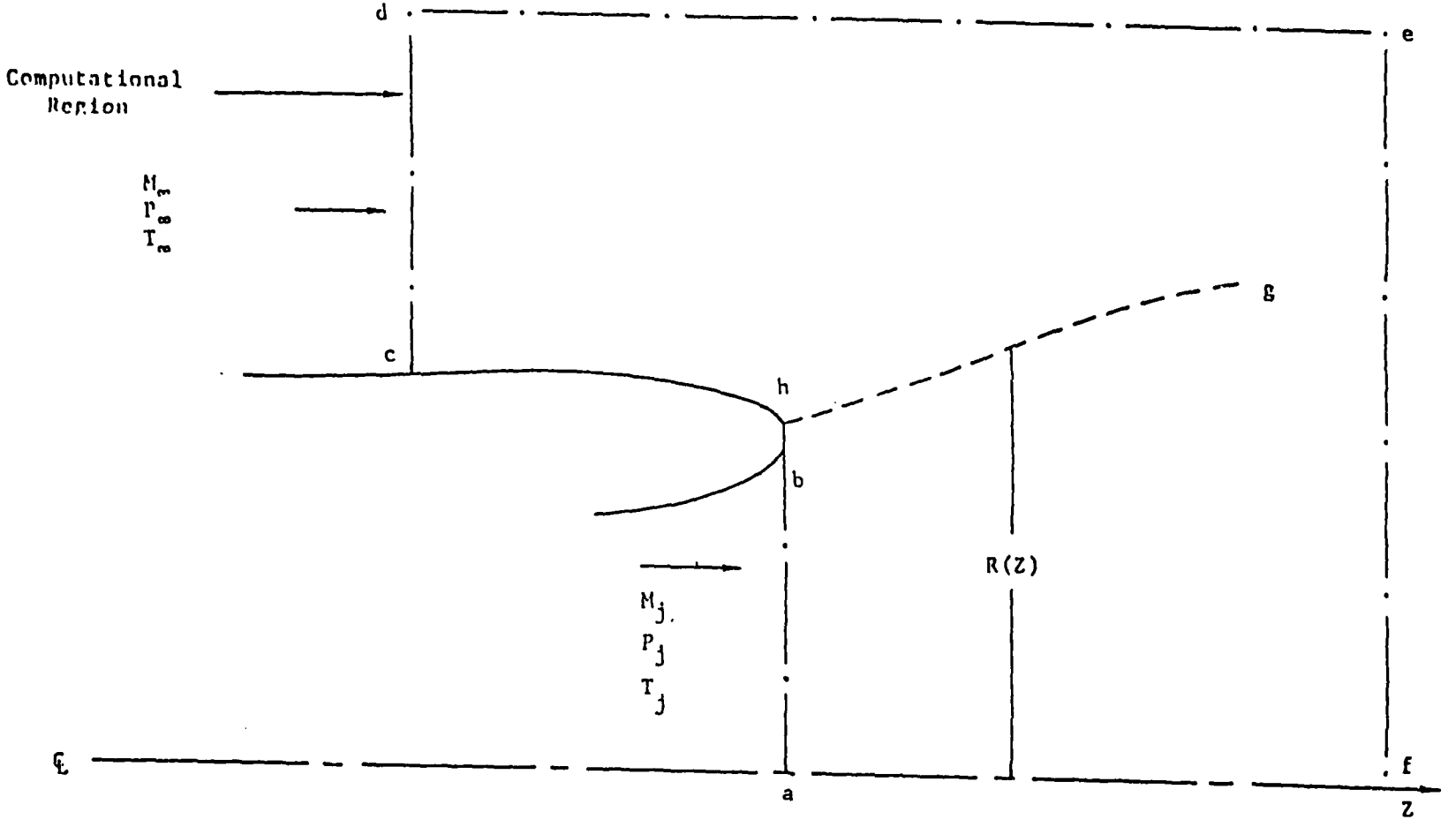

Figure 2 - Schematic of Computational Region.

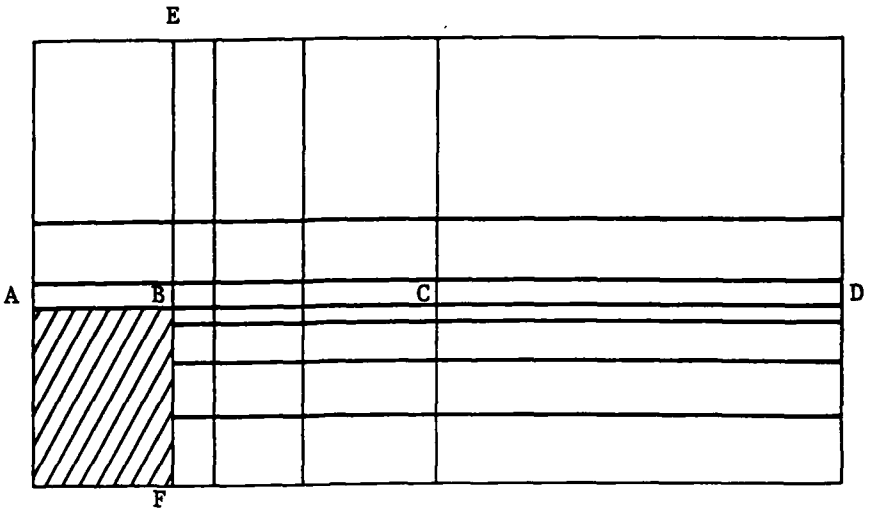

(a) Before Grid Movement

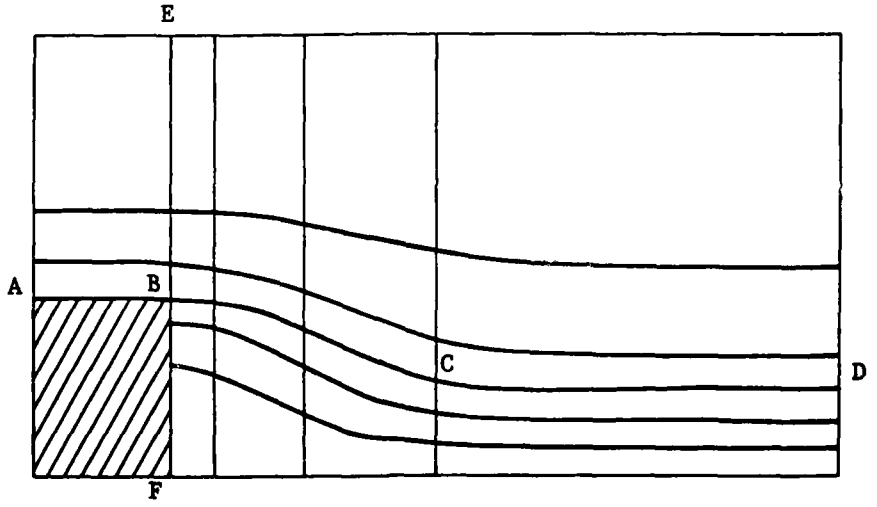

(b) After Grid Movement.

Figure 3 - Schematic of Adaptive Grid

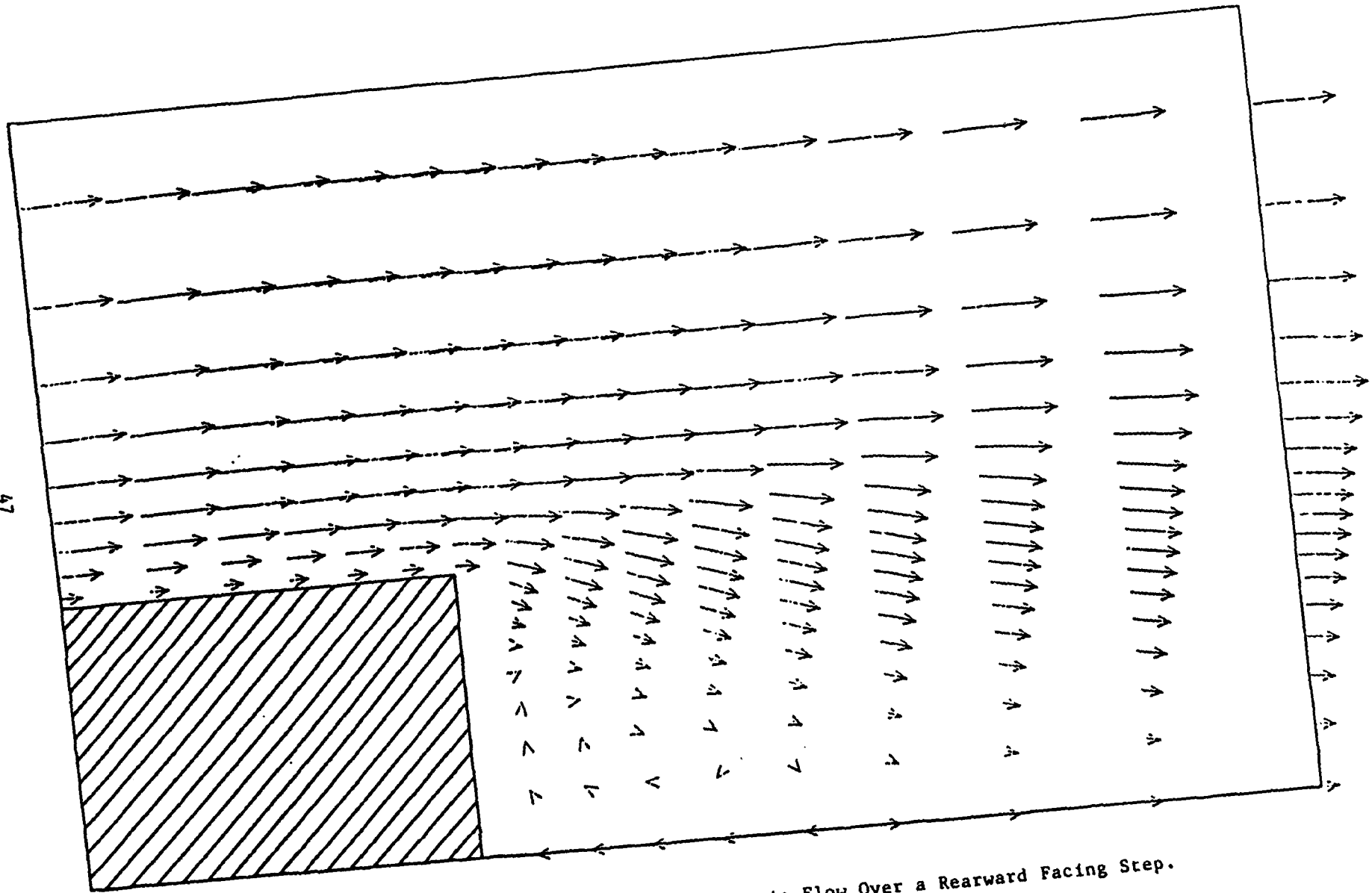

Figure 4. Velocity Vector Plot - Supersonic Flow Over a Rearward Facing Step.

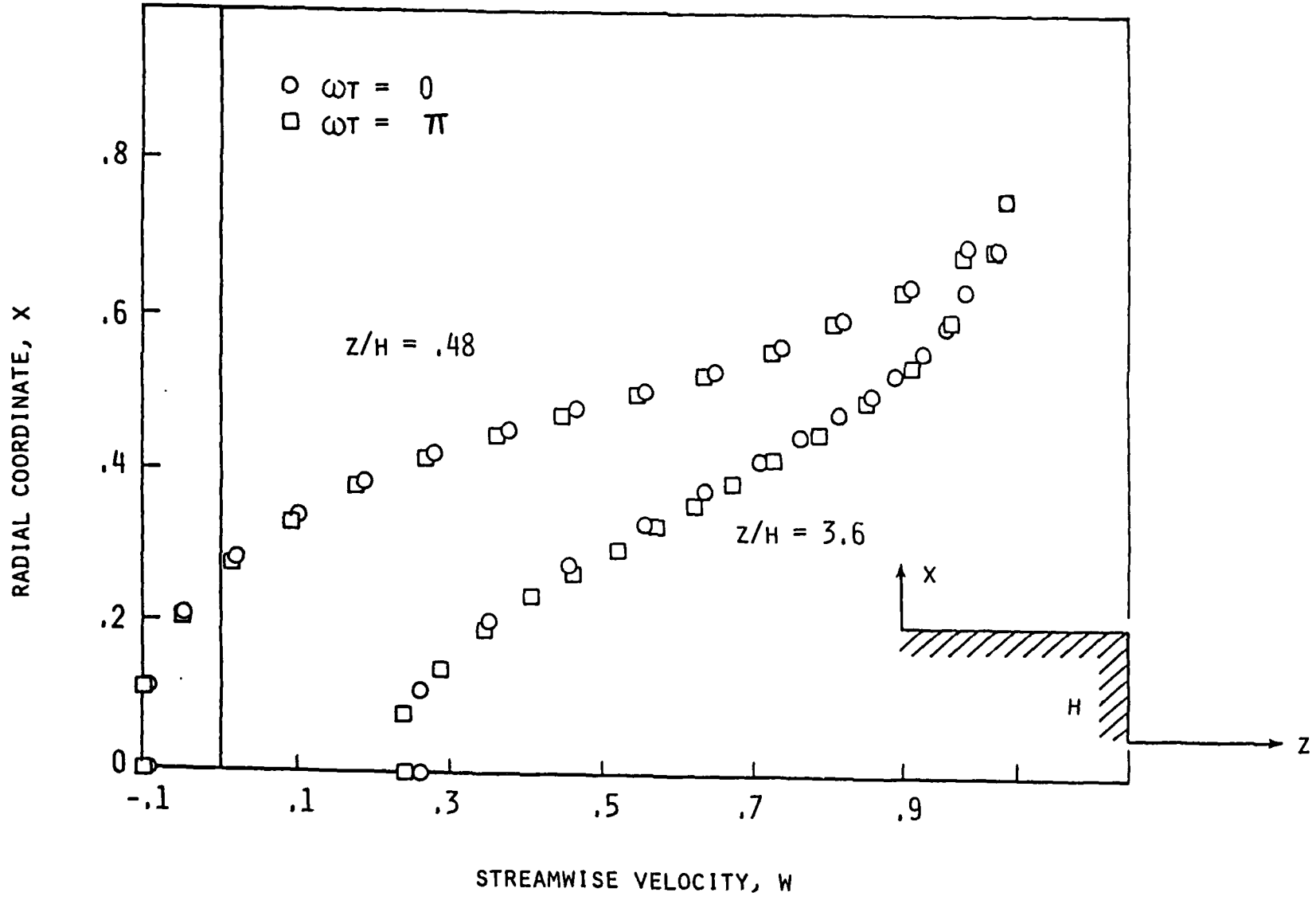

Figure 5 - Comparison of Streamwise Velocity Profiles During Forced Grid Movement.

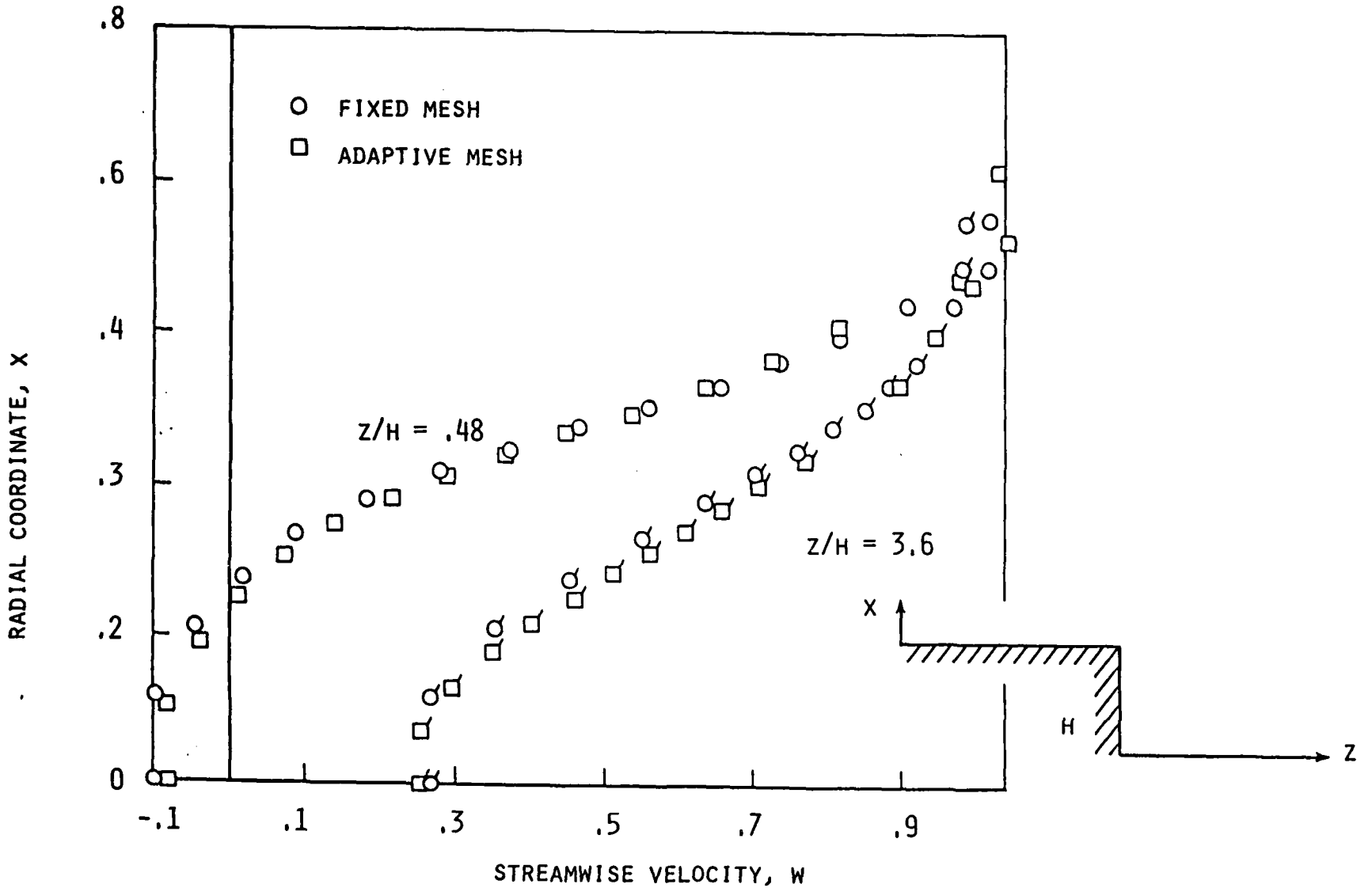

Figure 6 - Comparison of Fixed Mesh and Adaptive Mesh Calculations.

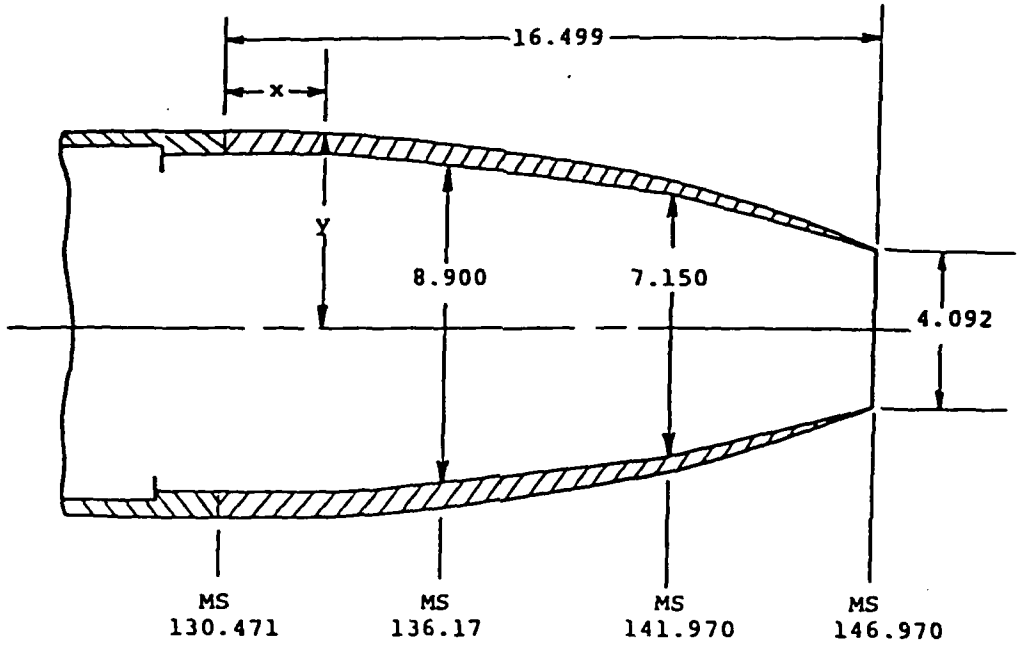

Stations and Dimensions in Inches

X	Y	X	Y	X	Y
0	4.930	5.653	4.624	11.322	3.760
0.230	4.926	5.899	4.595	11.569	3.707
0.476	4.923	6.146	4.565	11.815	3.653
0.723	4.918	6.392	4.536	12.062	3.592
0.969	4.915	6.639	4.504	12.308	3.530
1.216	4.913	6.885	4.472	12.555	3.464
1.462	4.908	7.132	4.440	12.801	3.397
1.709	4.903	7.378	4.407	13.048	3.326
1.955	4.895	7.625	4.376	13.294	3.252
2.202	4.889	7.871	4.341	13.541	3.173
2.448	4.881	8.118	4.304	13.787	3.089
2.695	4.874	8.364	4.267	14.034	3.002
2.941	4.864	8.611	4.228	14.280	2.914
3.188	4.854	8.857	4.191	14.527	2.820
3.434	4.841	9.104	4.154	14.773	2.726
3.681	4.824	9.350	4.115	15.020	2.626
3.927	4.807	9.597	4.075	15.266	2.524
4.174	4.785	9.843	4.036	15.513	2.419
4.420	4.760	10.090	3.993	15.636	2.366
4.667	4.736	10.336	3.949	15.759	2.315
4.913	4.711	10.583	3.905	16.006	2.214
5.160	4.684	10.879	3.858	16.252	2.125
5.406	4.654	11.076	3.809	16.499	2.046

Figure 7 - Nozzle Boattail Geometry (from Ref. 5).

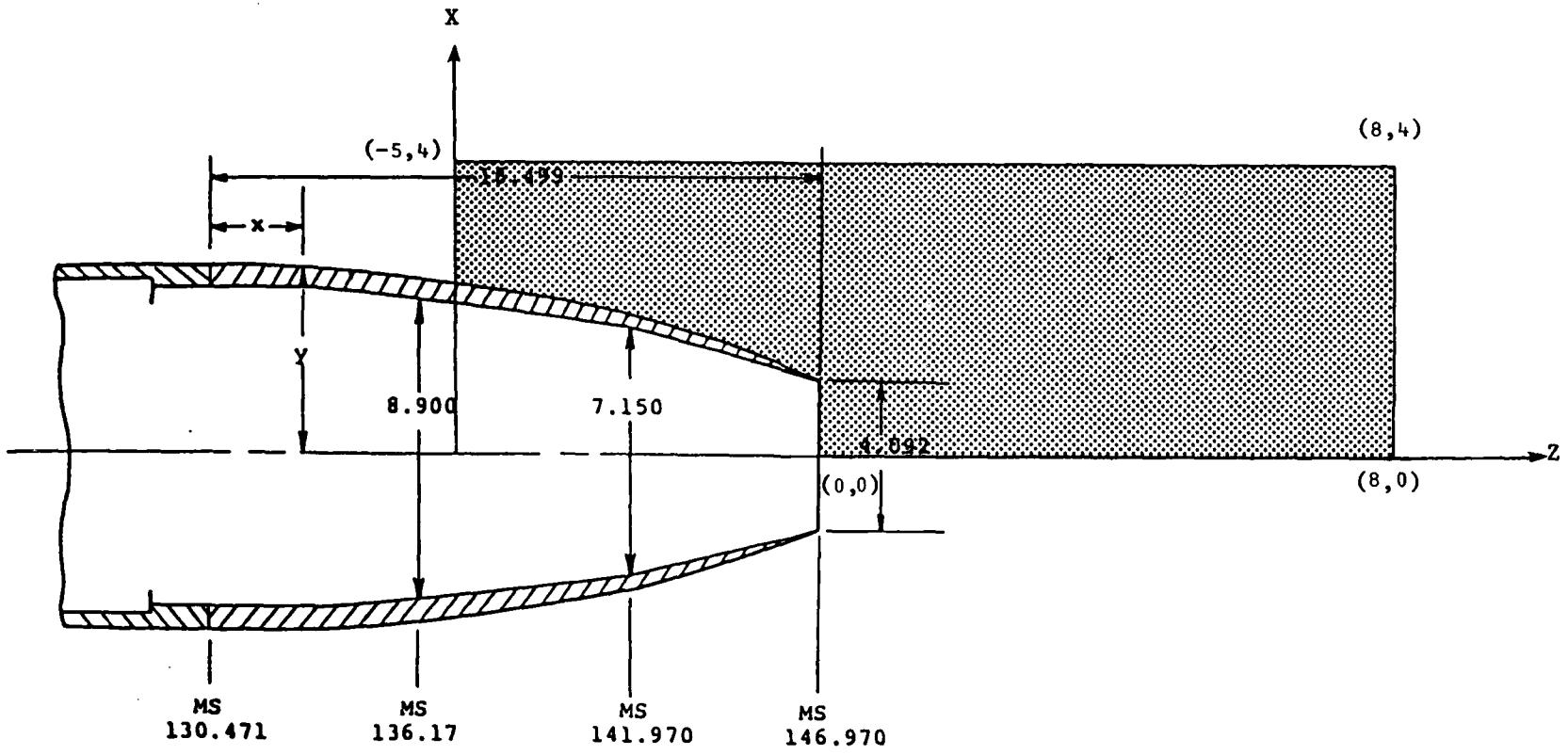

Figure 8 - Computational Domain for Nozzle Boattail Geometry.

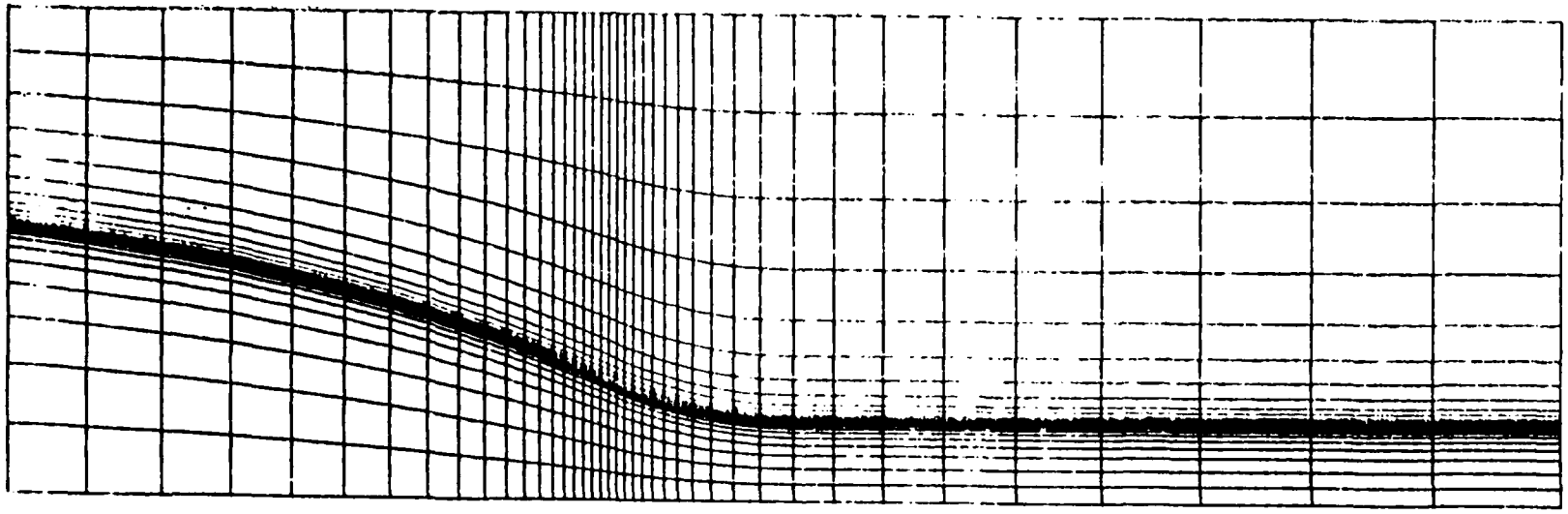

Figure 9 - Coordinate System - Full Domain.

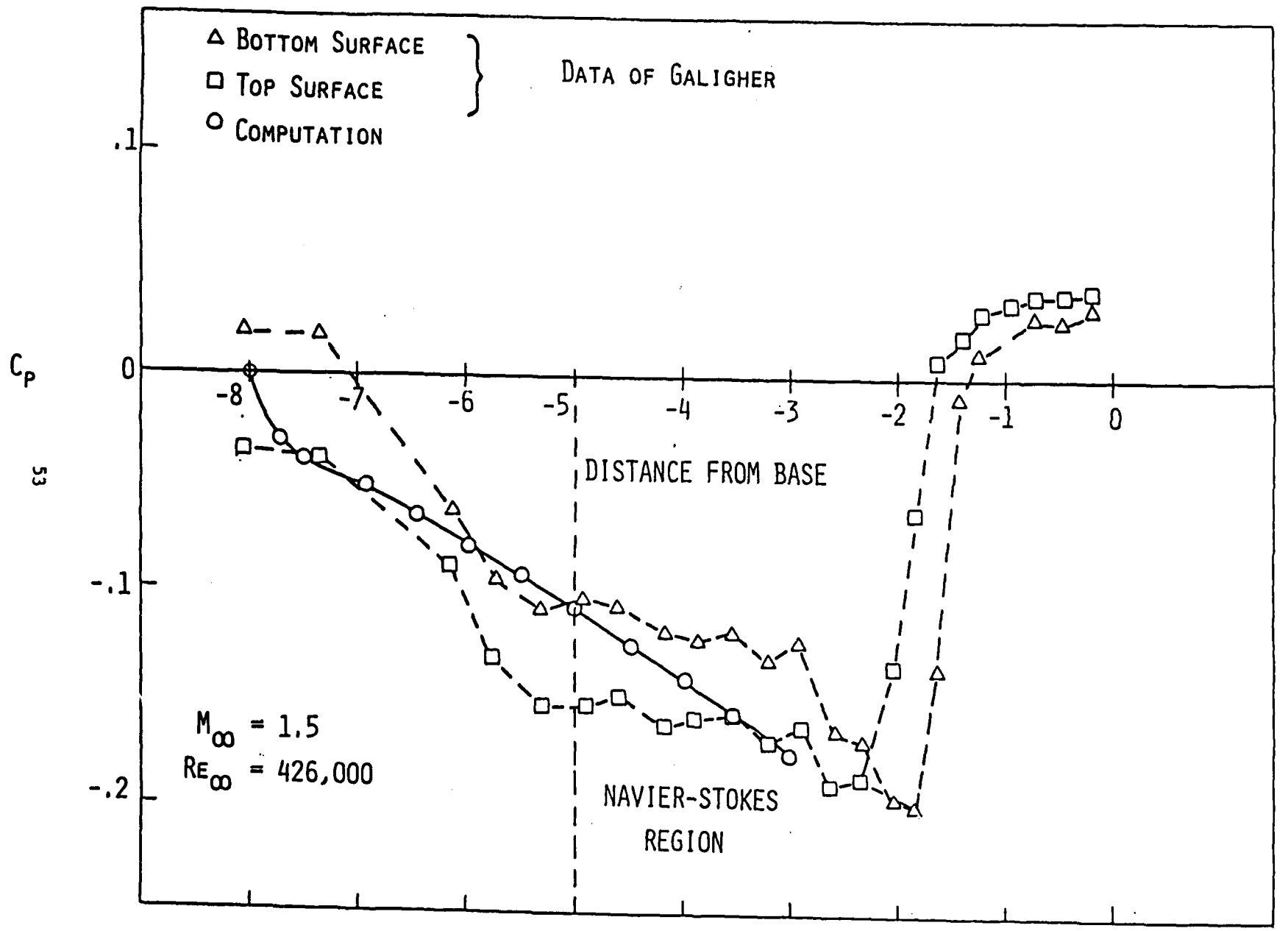

Figure 10 - Pressure Distribution on Shoulder of Boattail - "Upstream Boundary/Layer".

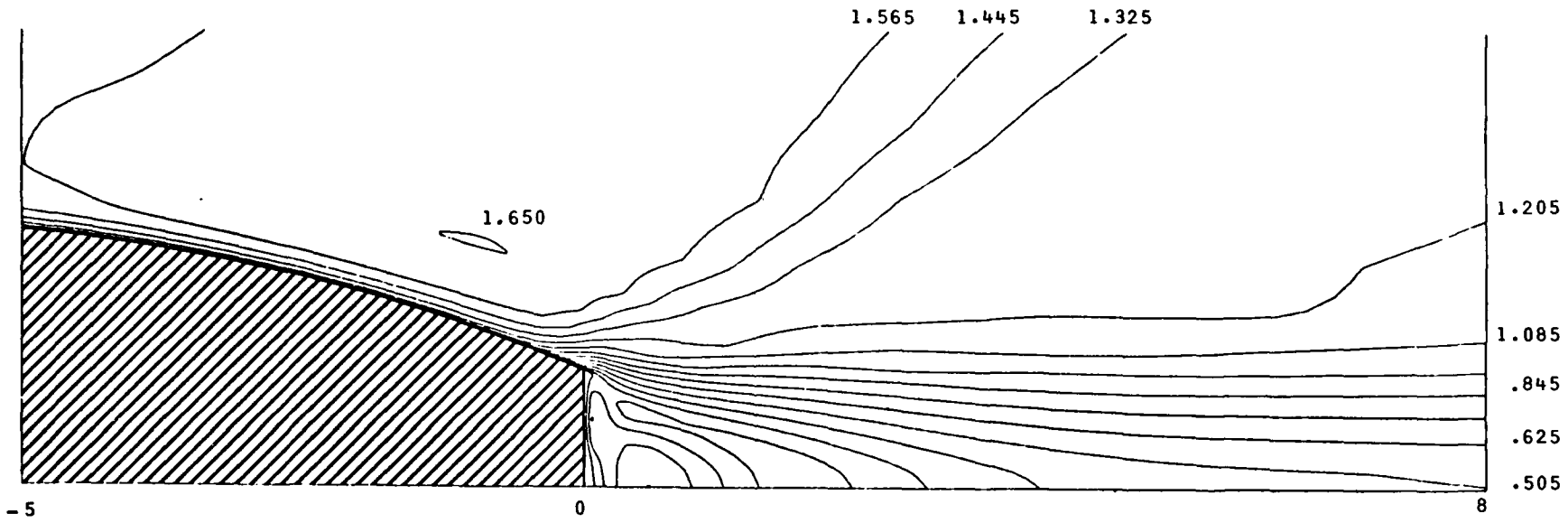

Figure 11 - Mach Number Contours - Jet off.

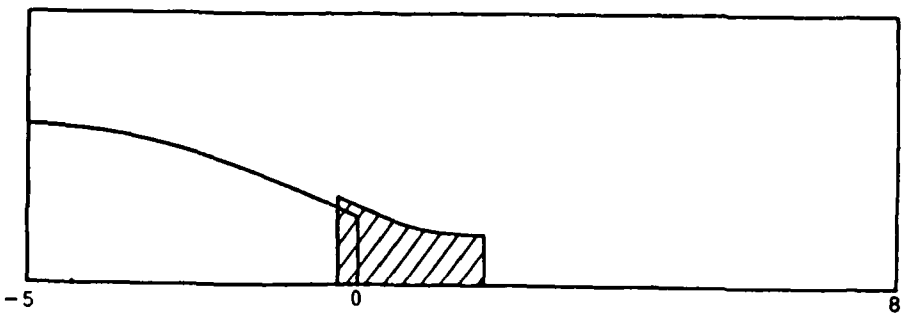

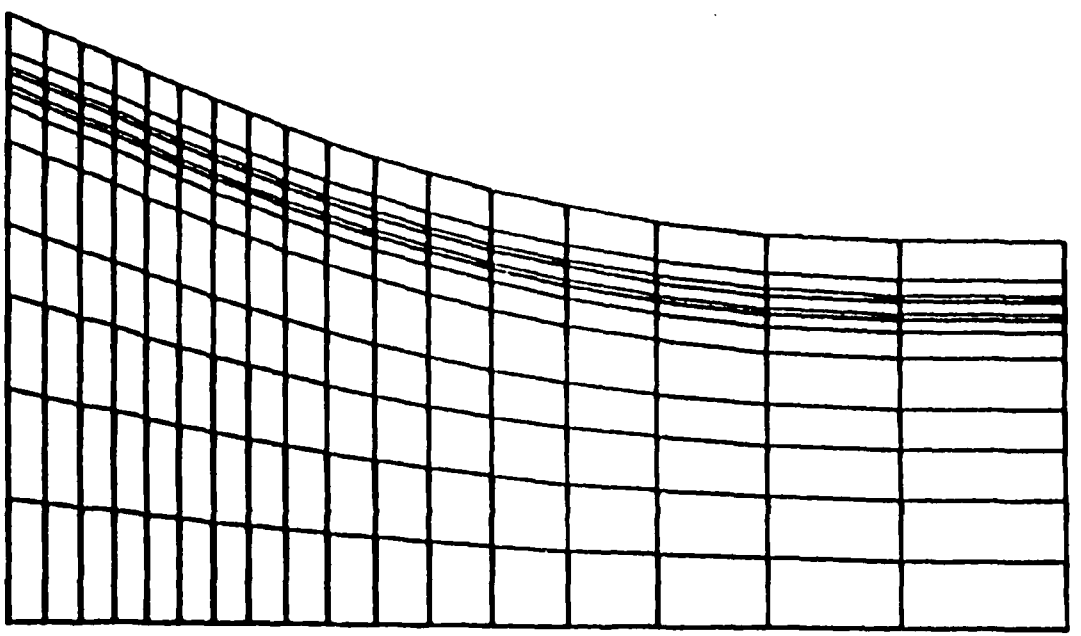

Figure 12 - Coordinates in Vicinity of Base.

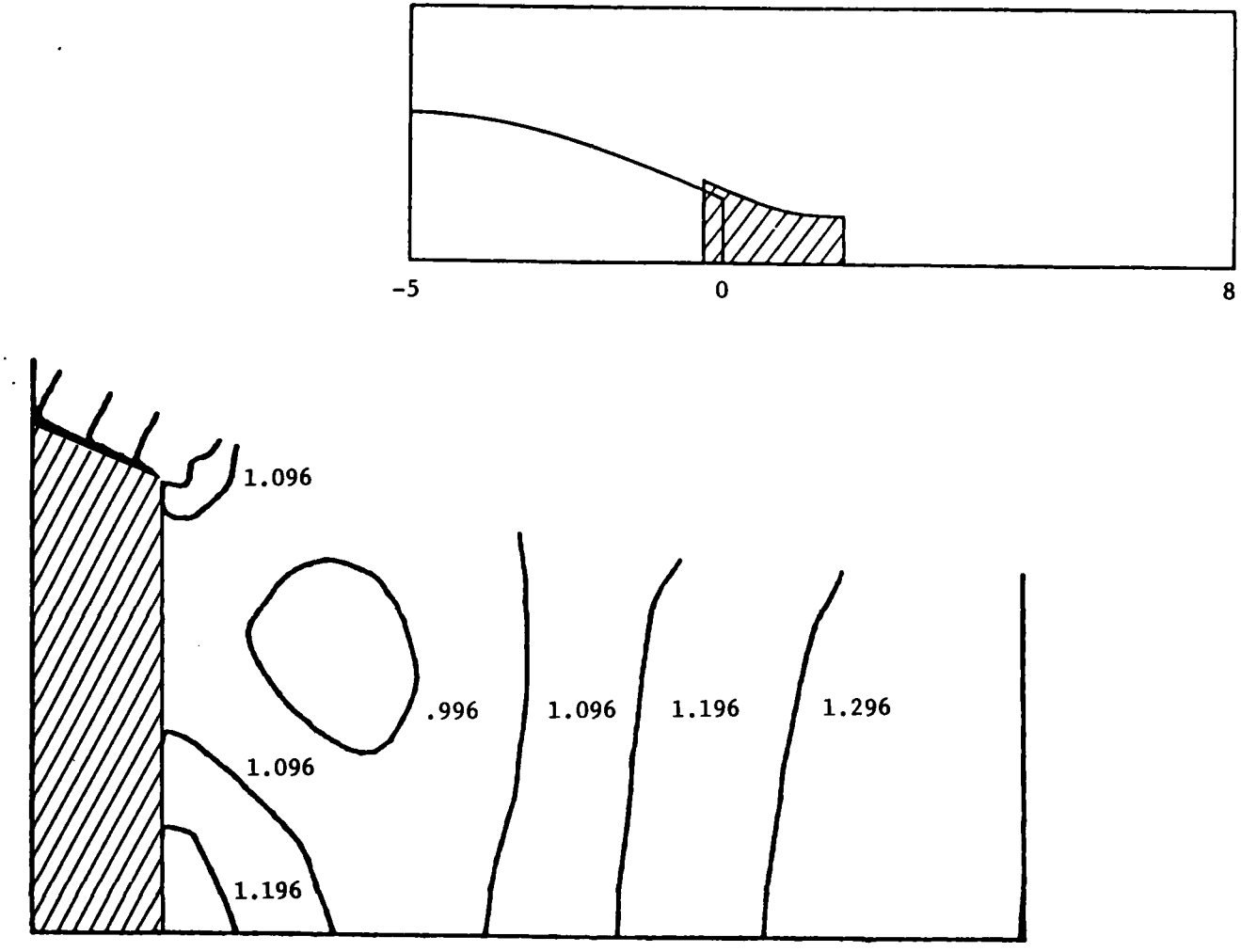

Figure 13 - Pressure Contours - Jet Off Conditions.

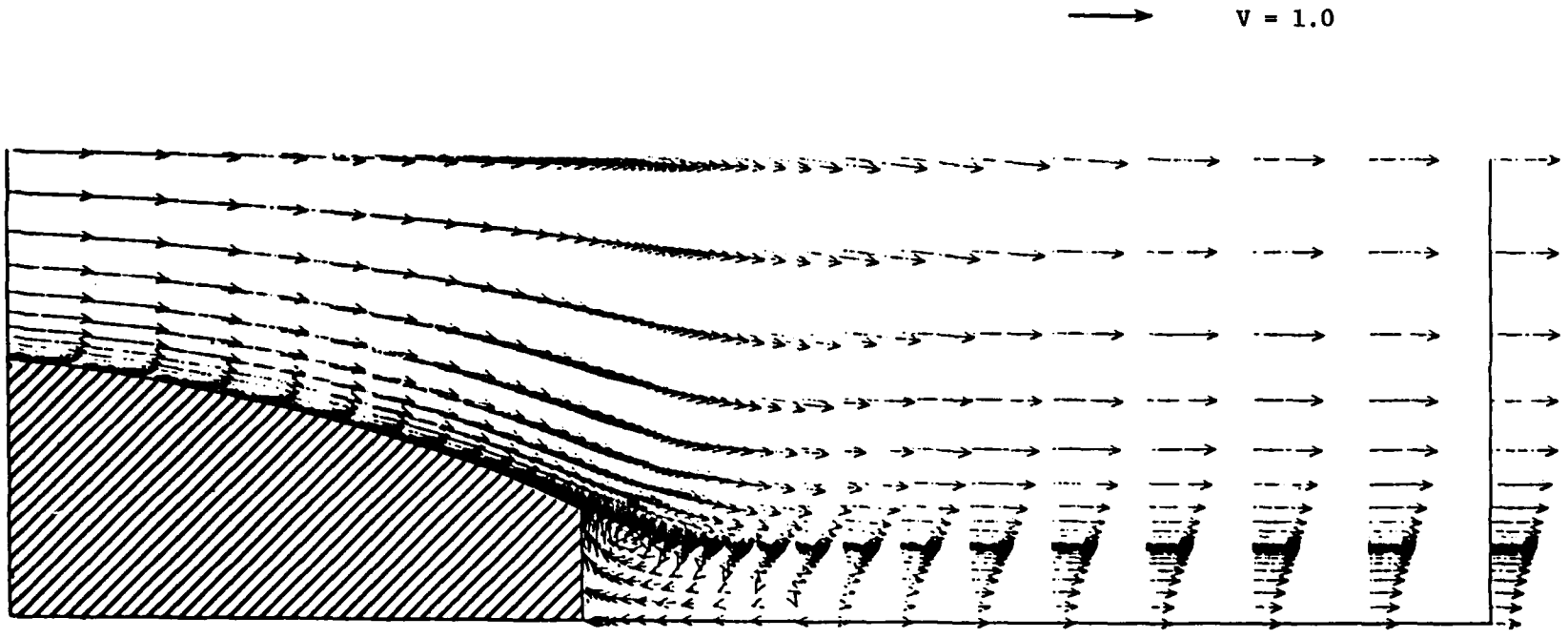

Figure 14 - Velocity Vector Plot - Jet Off.

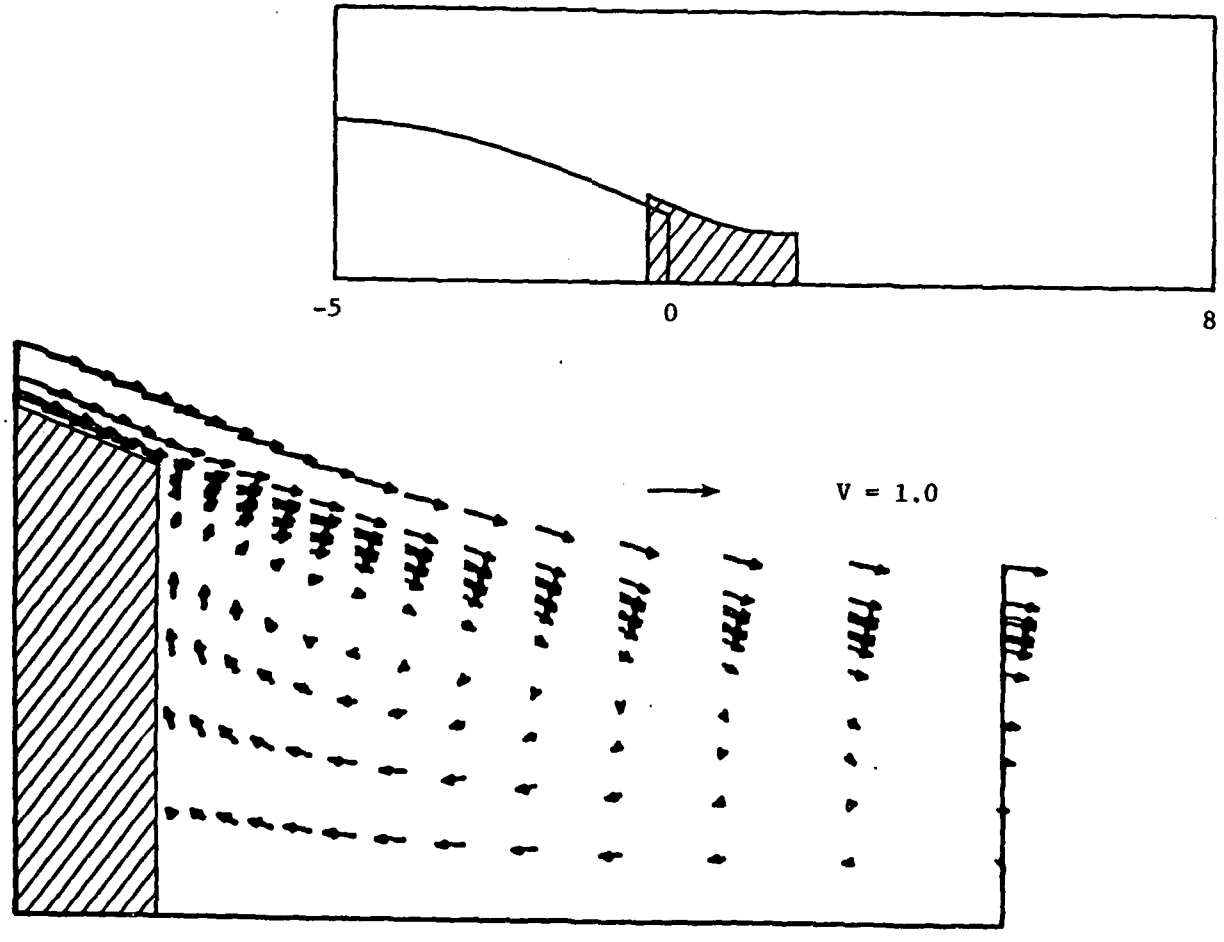

Figure 15 - Vector Plot - Jet Off Conditions.

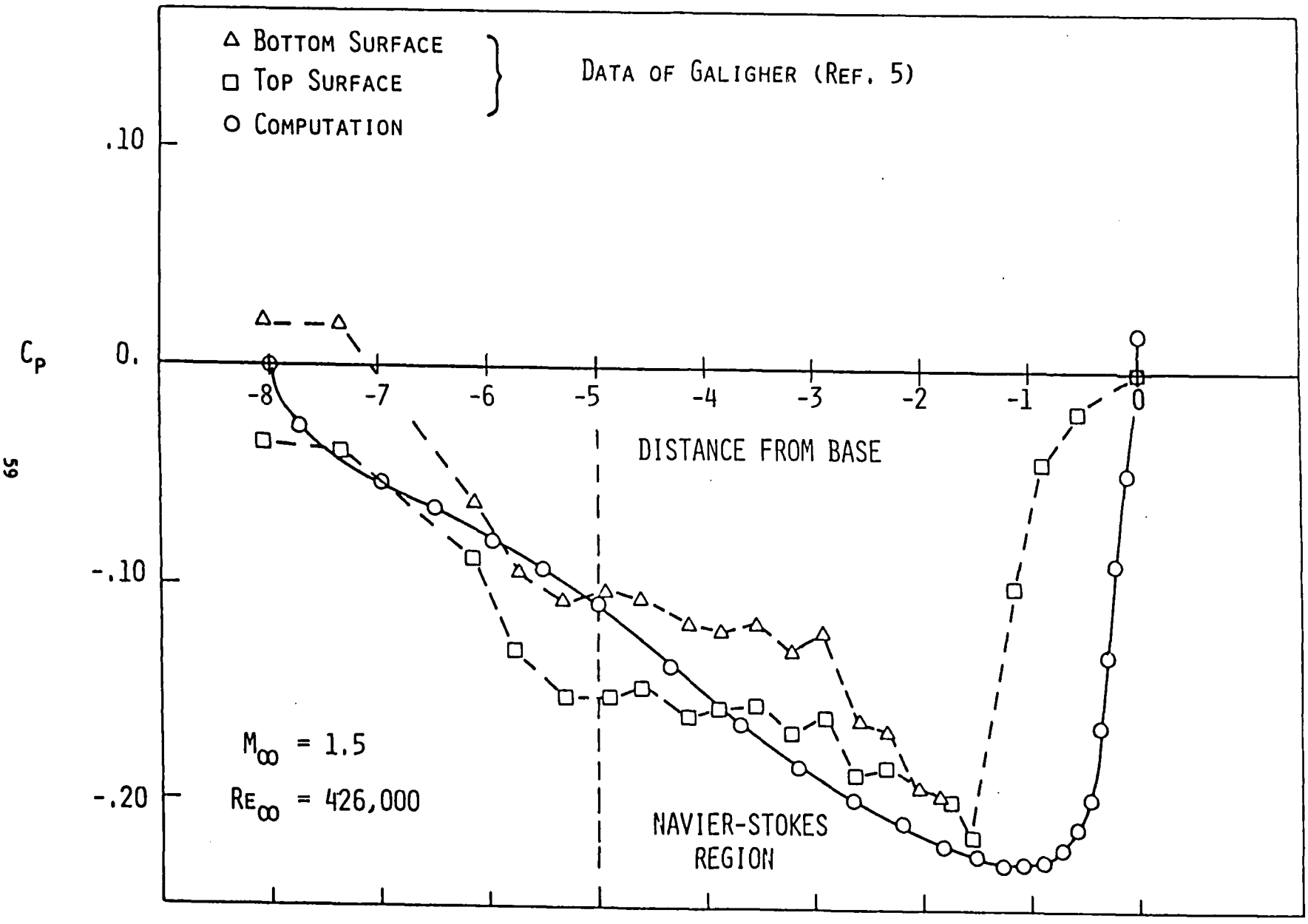

Figure 16 - Pressure Distribution on Shoulder of Boattail - Jet Off.

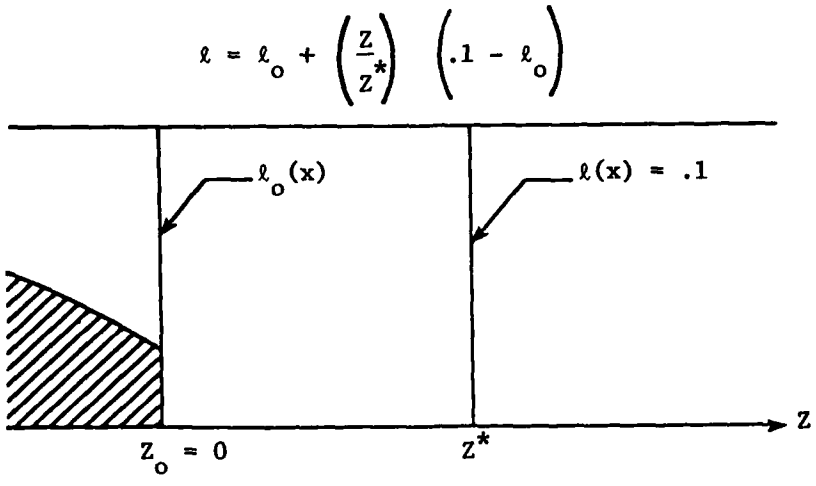

CASE	ℓ_{ω_o}	Z^*	$C_P(Z_o)$	FROZEN AT
1	.02481	FROZEN	.112	$P_{MINIMUM}$
2	.04040	3.415	.069	SEPARATION PT.
3	.02504	1.044	.039	$P_{MINIMUM}$
4	.02504	.575	.018	$P_{MINIMUM}$

Figure 17 - Effect of Length Scale in Wake Region on Boattail Corner Pressure Jet Off Case.

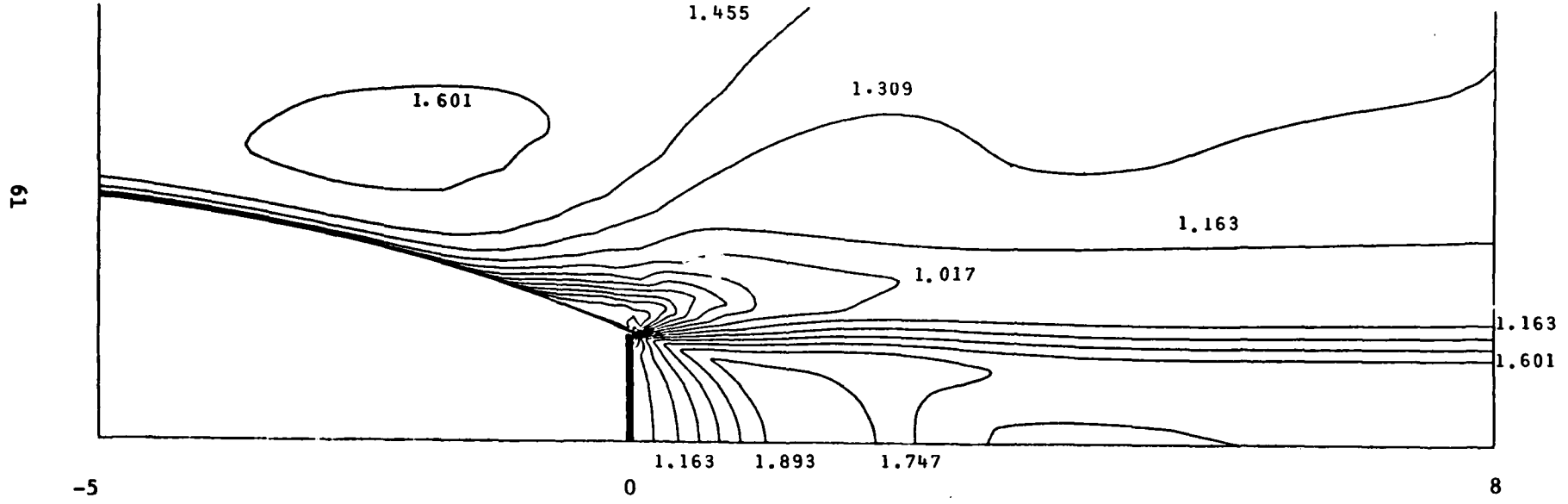

Figure 18 - Mach Number Contours - Jet On.

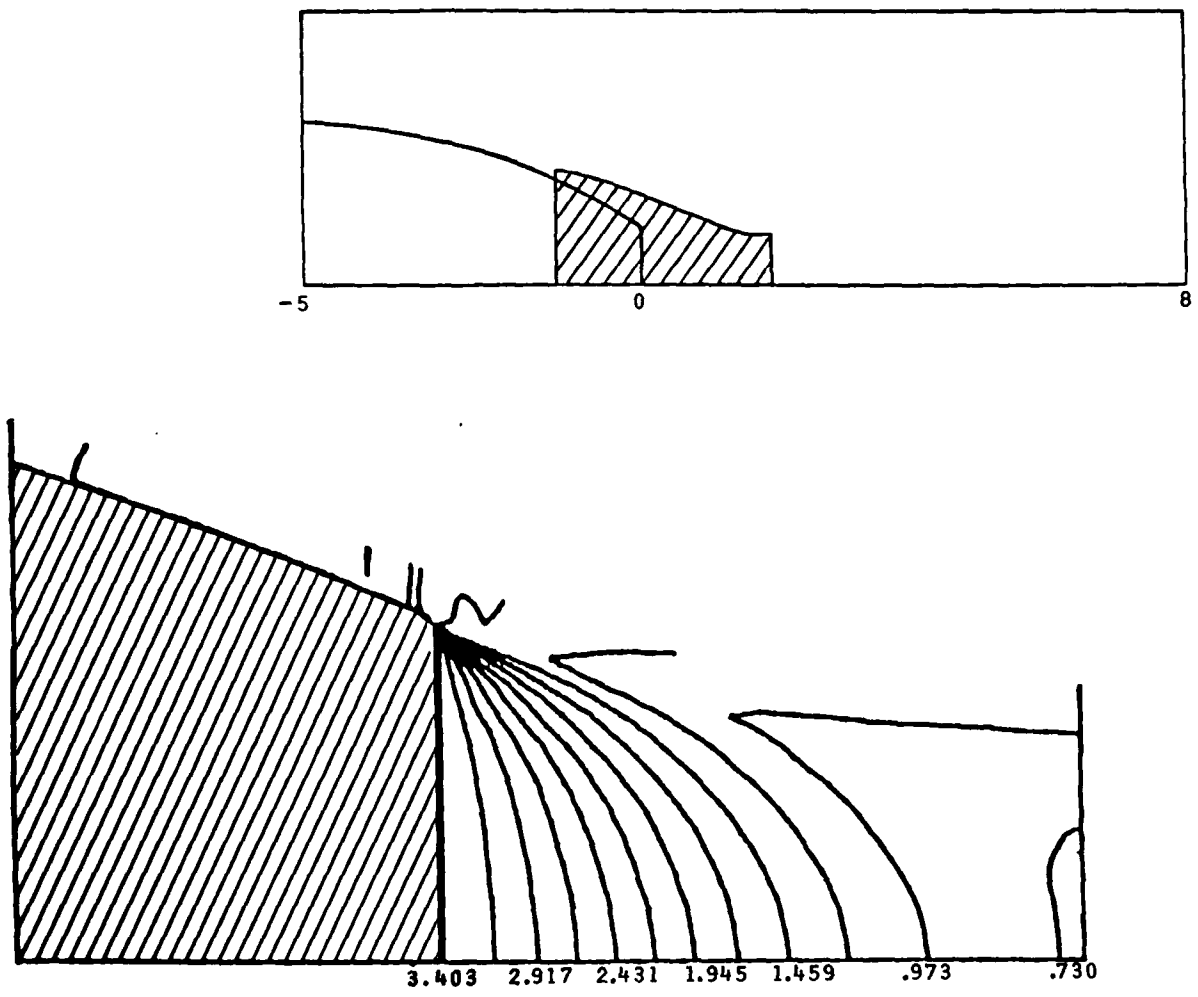

Figure 19 - Pressure Contours - Jet On Conditions.

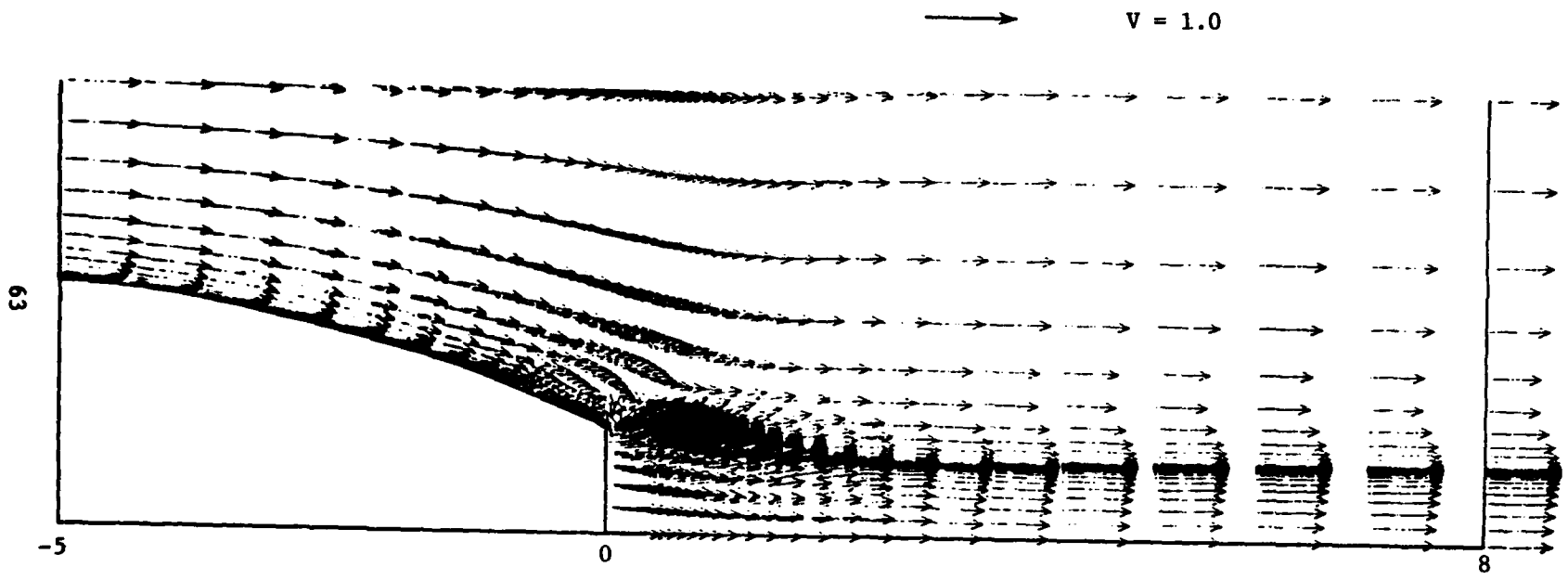

Figure 20 - Velocity Vector Plot - Jet On.

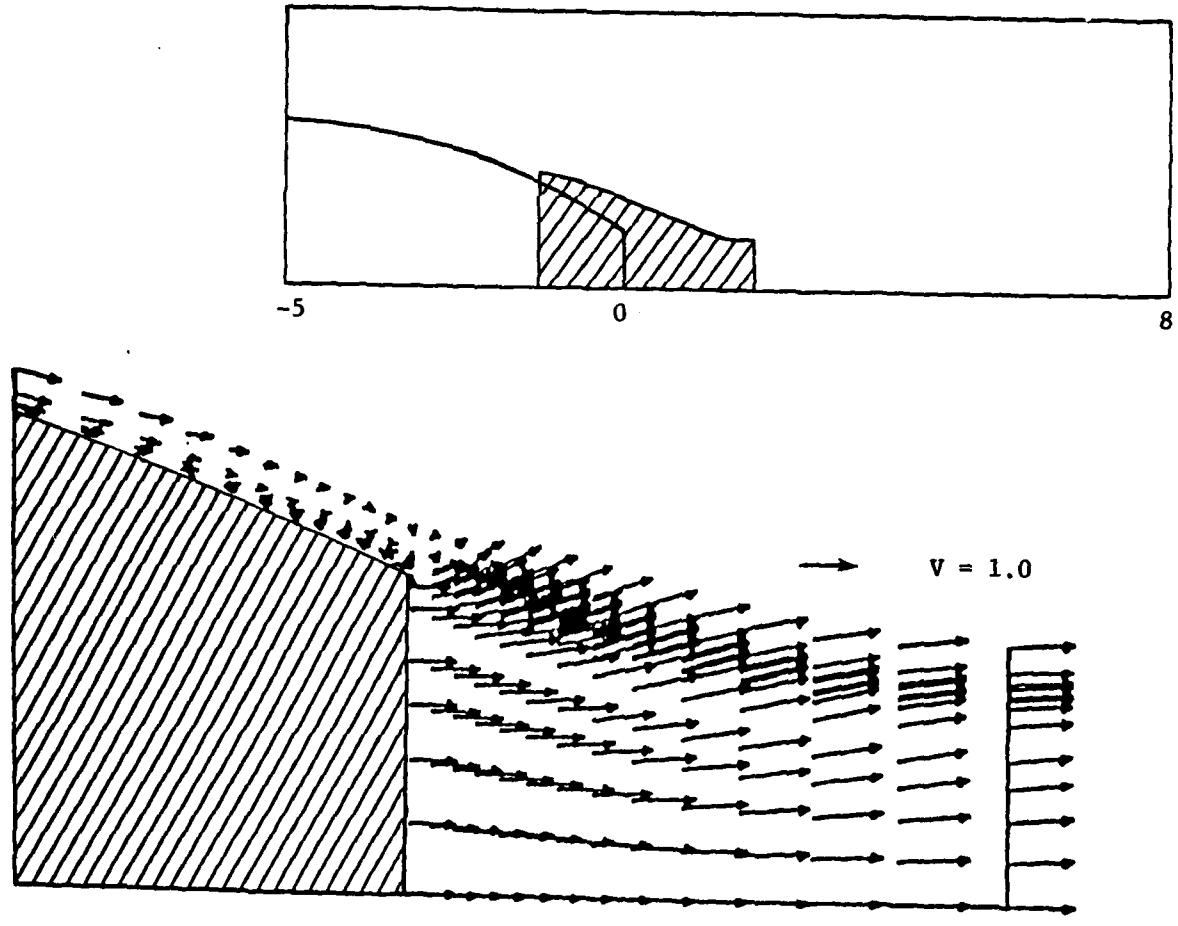

Figure 21 - Vector Plot - Jet On Conditions.

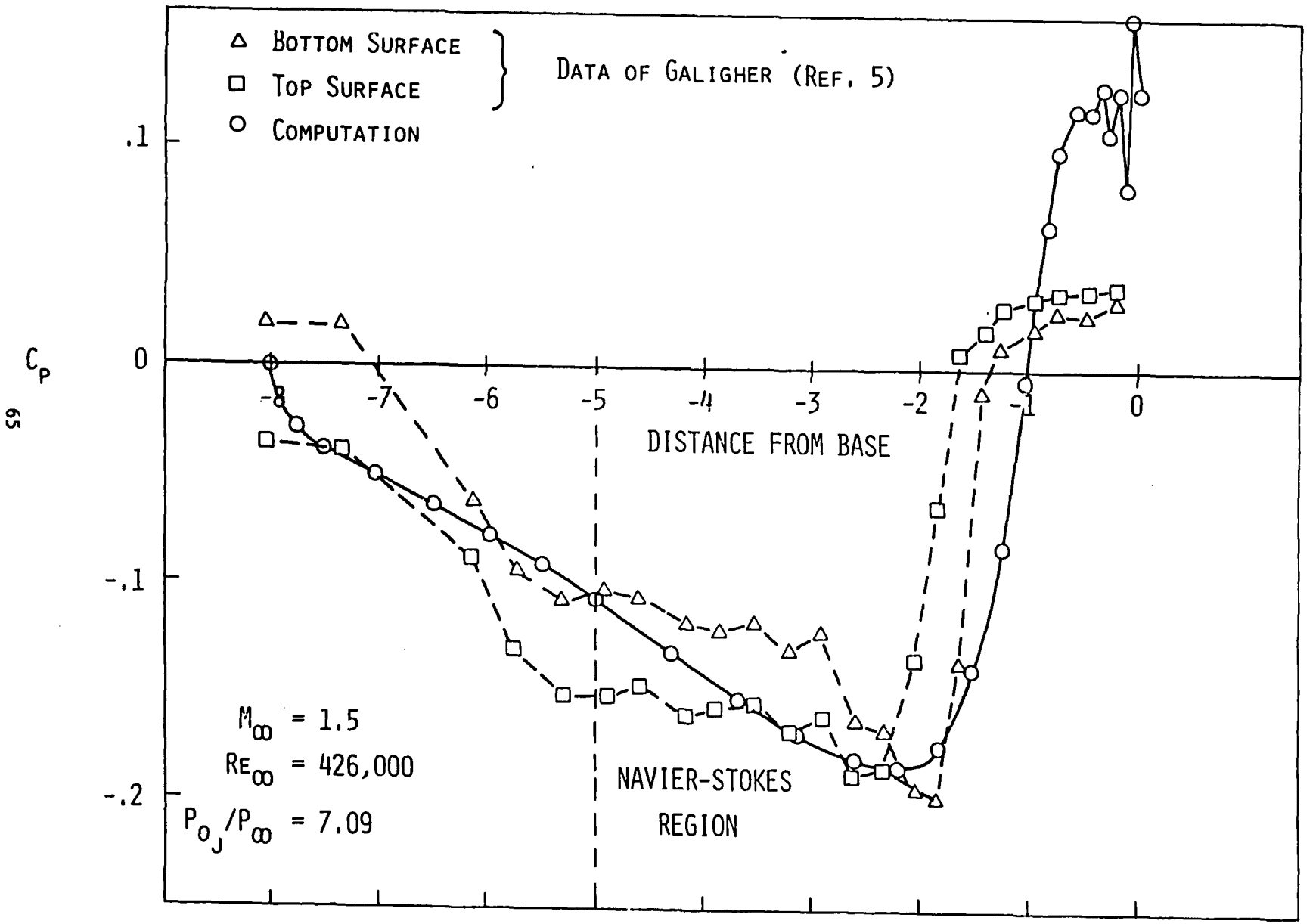

Figure 22 - Pressure Distribution on Shoulder of Boattail - Jet On.

CASE 8641 (SETTLES, BACA, WILLIAMS, BOGDONOFF, 1980)

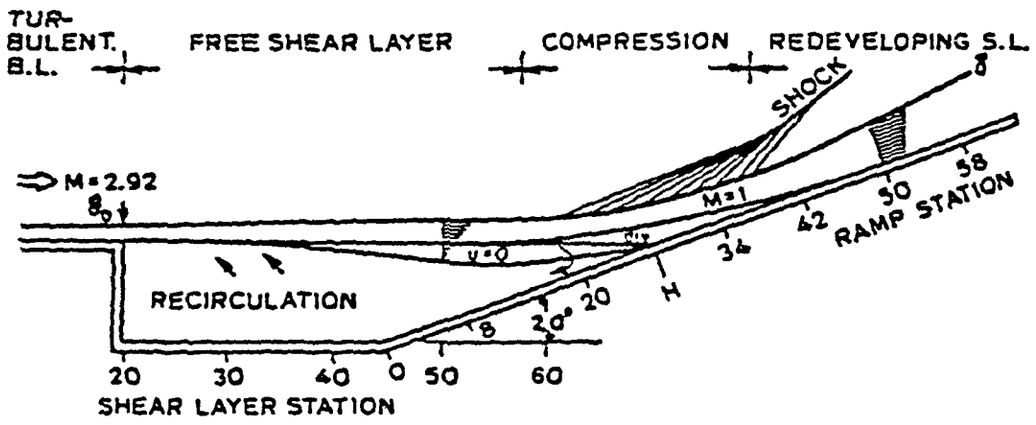

10 units = 3.94 cm

Figure 23 - Schematic of Flow Field.

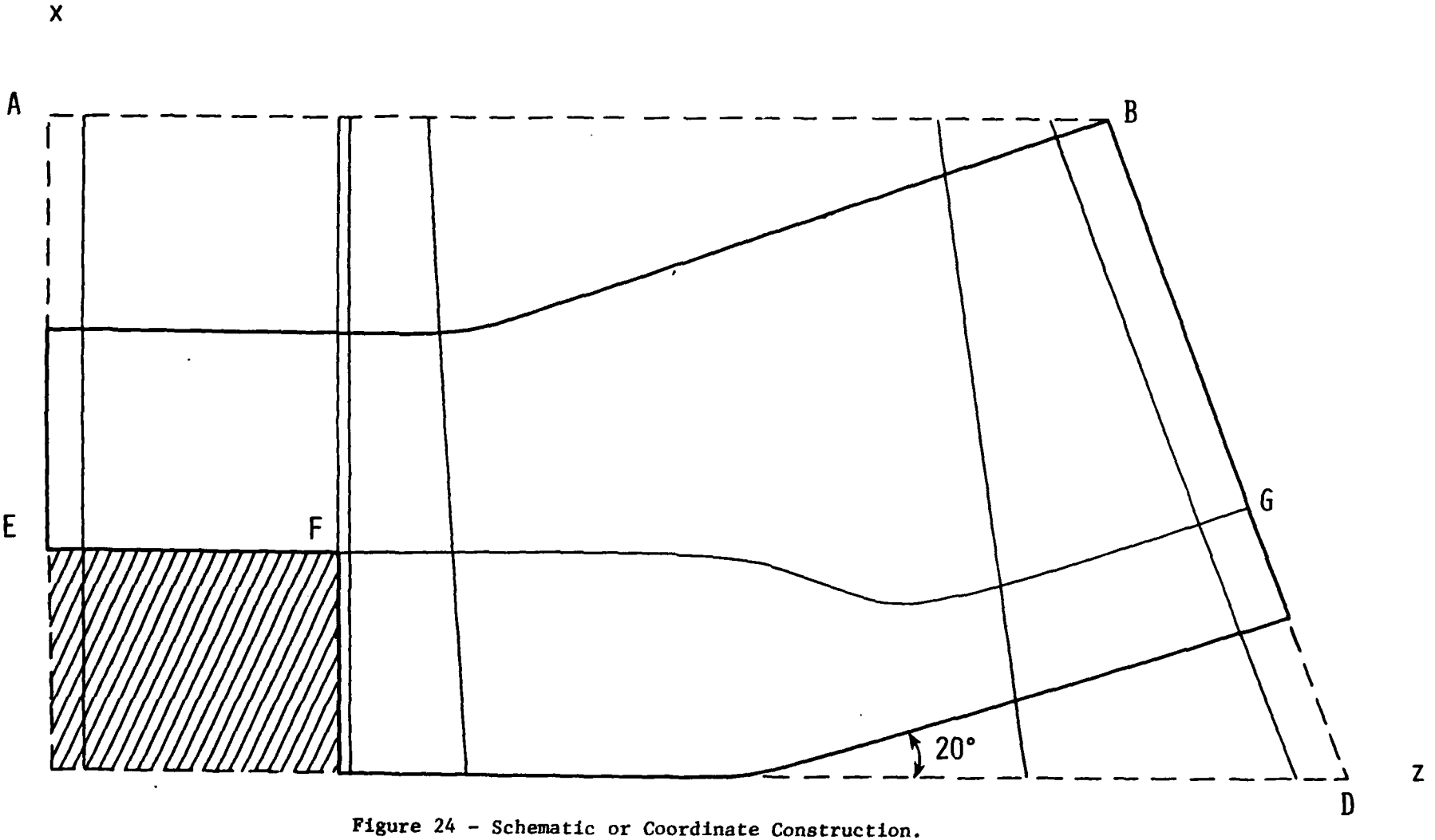

Figure 24 - Schematic or Coordinate Construction.

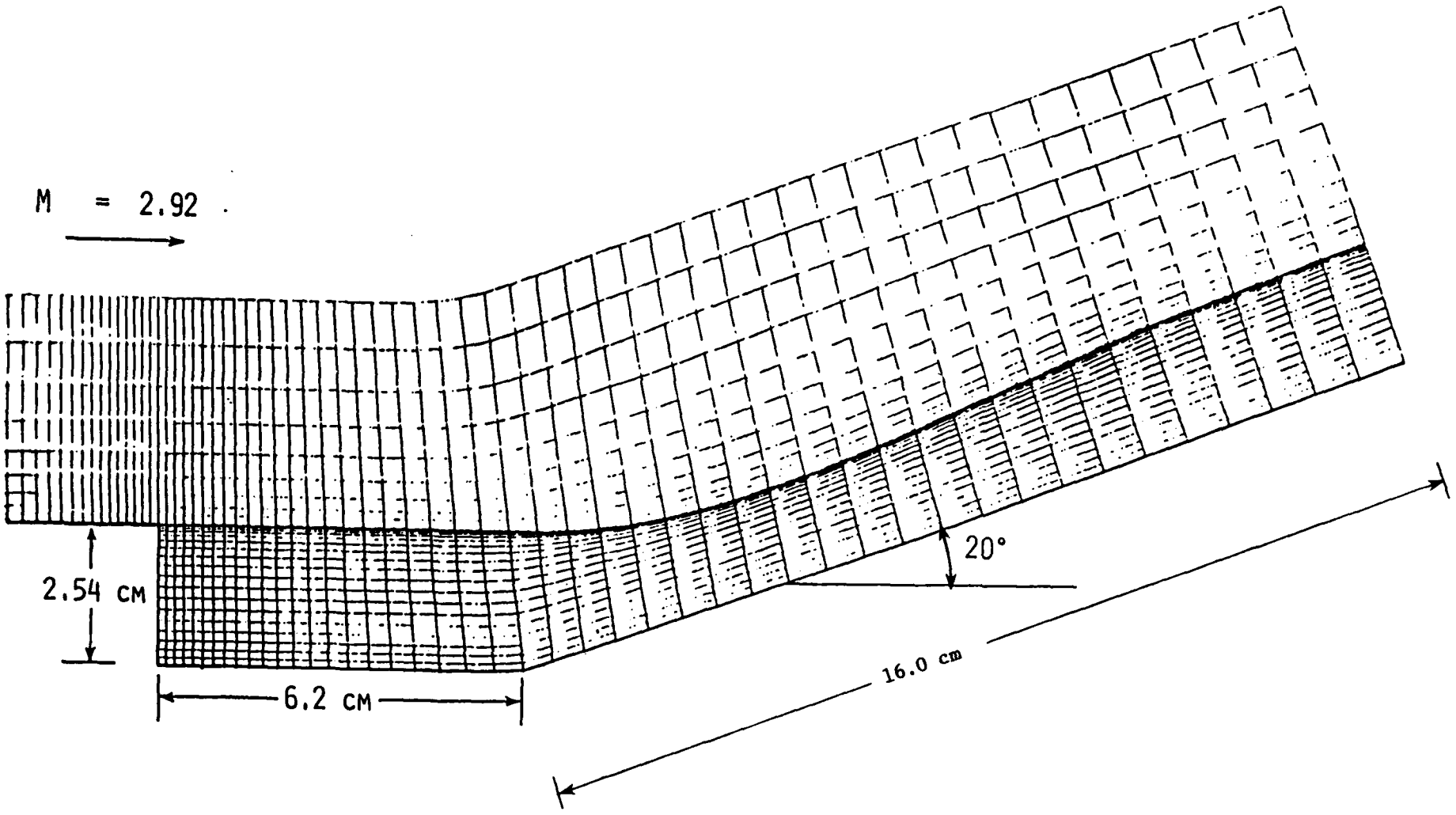

Figure 25 - Computational Domain.

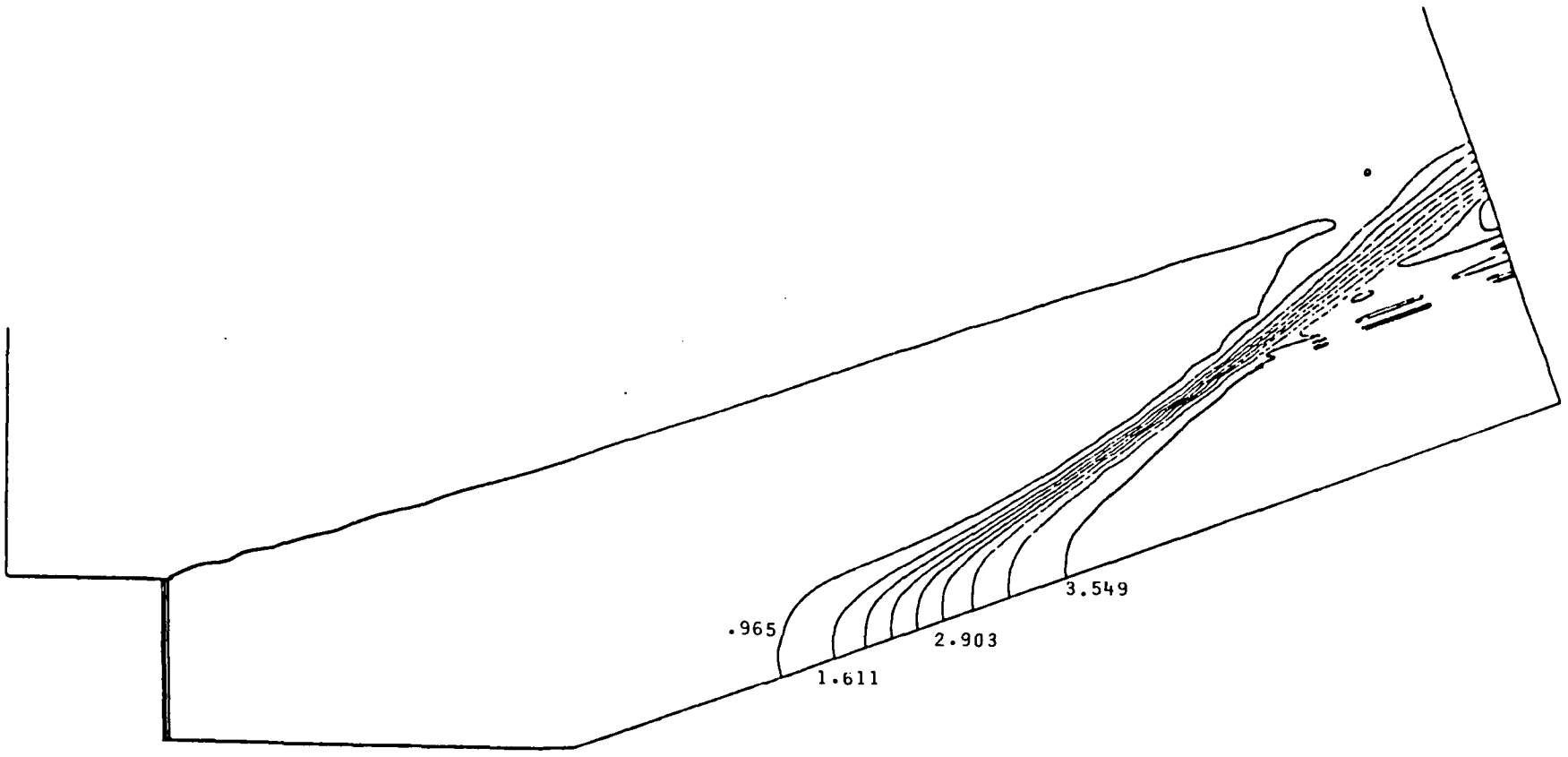

Figure 26 - Computed Contour Plot of Pressure.

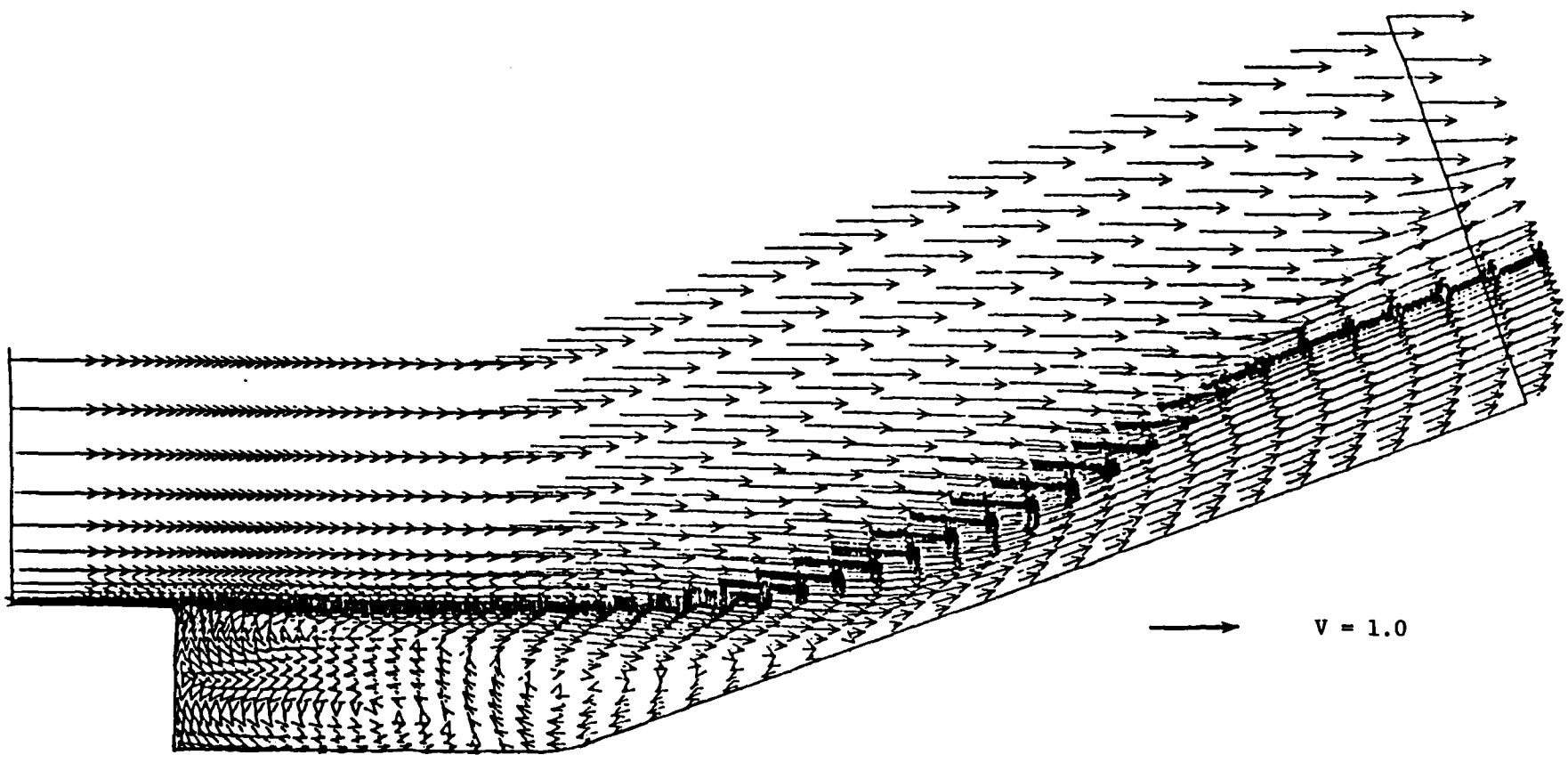

Figure 27 - Computed Vector Plot.

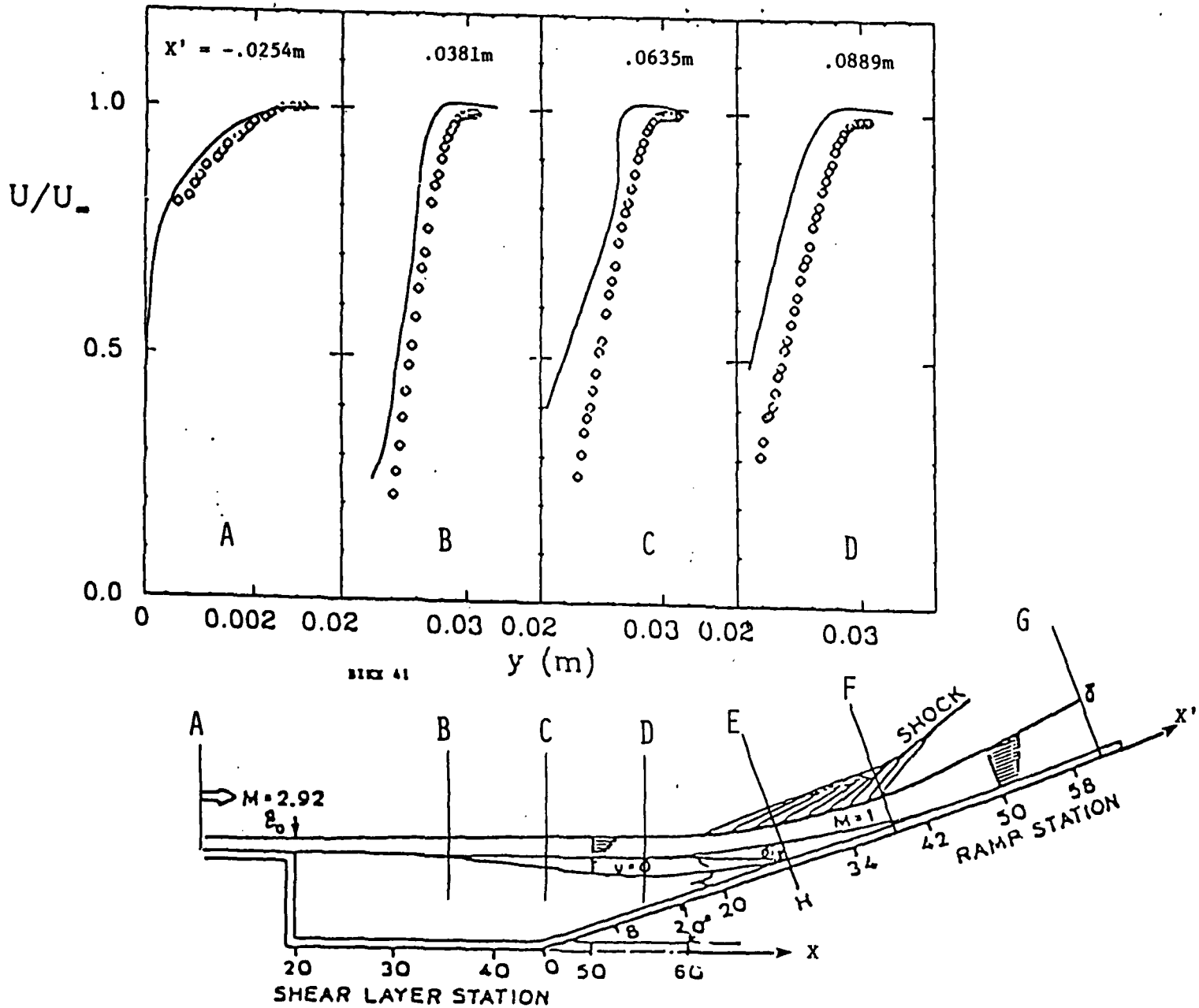

Figure 28 - Velocity Profiles Through Shear Layer.

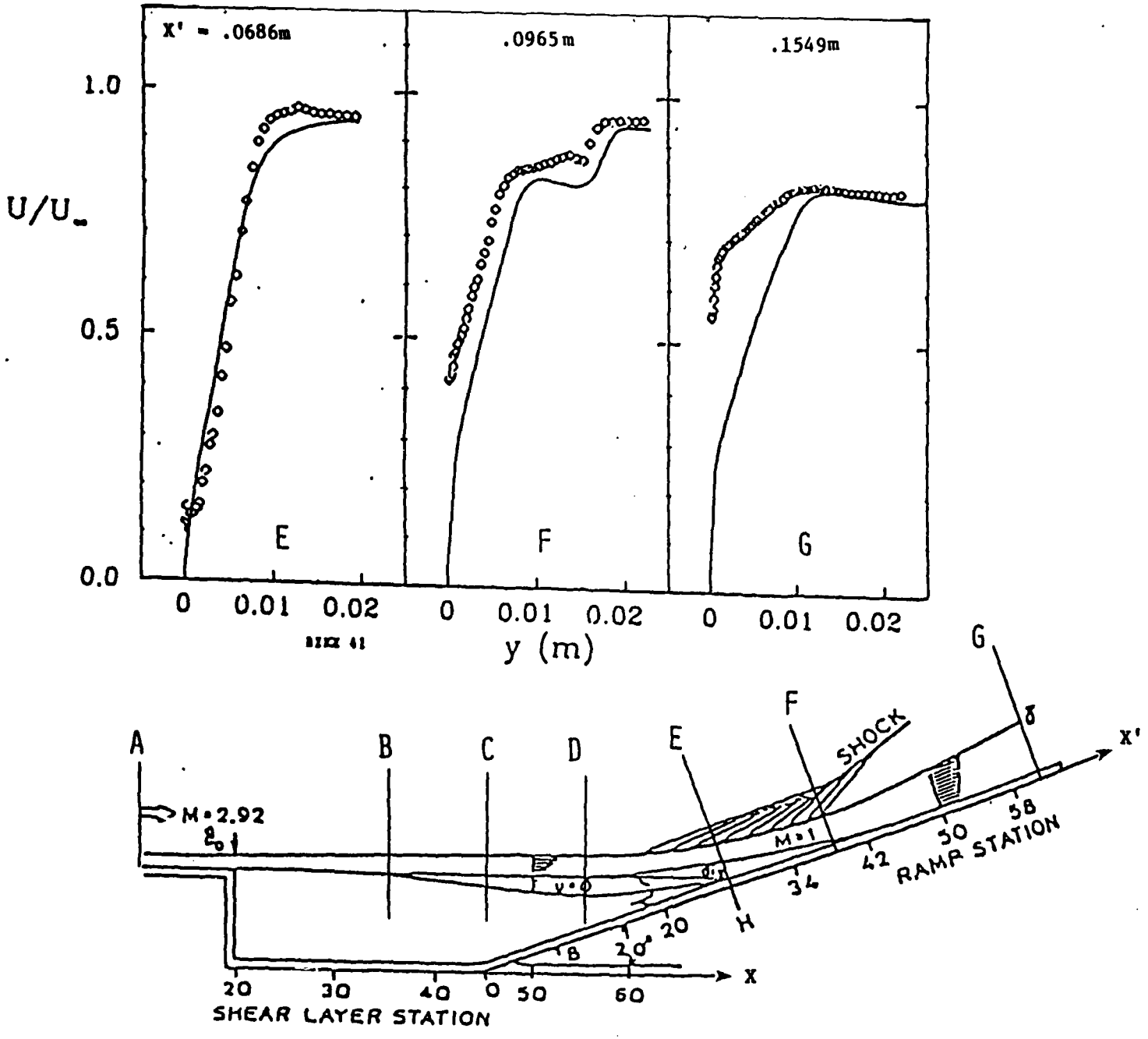

Figure 29 - Velocity Profiles on Ramp.

REFERENCES

1. Batiuk, G.: A Bibliography of Plume Effects Investigations Conducted by the Army Missile Command. U.S. Army Missile Command, Technical Report RD-76-16, 1976.

2. Shrewsbury, G.D.: Effect of Boattail Juncture Shape on Pressure Drag Coefficients of Isolated Afterbodies. NASA TM X-1517, 1968.

3. Strike, W.T.: Jet Plume Simulation at Mach Number 10. AEDC-TR-70-118, 1970.

4. Alpinieri, L.J. and Adams, R.H.: Flow Separation Due to Jet Pluming. AIAA Journal, Vol. 4, 1966.

5. Galigher, L.L., Yaros, S.F. and Bauer, R.C.: Evaluation of Boattail Geometry and Exhaust Plume Temperature Effects on Nozzle Afterbody Drag at Transonic Mach Numbers, Arnold Engineering Development Center, AEDC-TR-76-102, Oct. 1976.

6. Burt, J.R.: An Investigation of the Effectiveness of Several Devices in Simulating a Rocket Plume at Free Stream Mach Numbers of 0.9 to 1.2. U.S. Army Missile Command, Technical Report RD-TR-71-22, 1971.

7. Crocco, L. and Lees, L.: A Mixing Theory for Interaction Between Dissipative Flows and Nearly Isentropic Streams. Journal of the Aeronautical Sciences, Vol. 19, October, 1962.

8. Reeves, B. and Lees, L.: Theory of Laminar Near Wake of Blunt Bodies in Hypersonic Flow. AIAA Journal, Vol. 3, November, 1965.

9. Baum, E. and Denison, R.: Interacting Supersonic Laminar Wake Calculations by a Finite Difference Method. AIAA Paper No. 66-45, 1966.

10. Alber, I. and Lees, L.: Integral Theory for Supersonic Turbulent Base Flow. AIAA Journal, Vol. 6, July, 1968.

11. Shamroth, S.J. and McDonald, H.: A New Solution of the Turbulent Near-Wake Recompression Problem. The Aeronautical Quarterly, Vol. 23, May 1972.

12. Korst, H.H., Page, R.H. and Childs, M.E.: A Theory for Base Pressure in Transonic and Supersonic Flow. University of Illinois Engineering Experimental Station, M. E. TN 392-2, 1955.

13. Chapman, D.R.: An Analysis of Base Pressure at Supersonic Velocities and Comparison with Experiments. NACA TN 2137, 1950.

14. Page, R.H., Hill, W.G. and Kessler, T.J.: Reattachment of Two-Dimensional Supersonic Turbulent Flows. ASME Paper 67-FE-20, May 1967.

15. Page, R.H.: A Review of Component Analysis of Base Pressure for Supersonic Turbulent Flow. Proceedings of the Tenth International Symposium on Space Technology and Science. Tokyo, 1973.

16. Allen, J.S. and Cheng, S.I.: Numerical Solution of the Compressible Navier-Stokes Equations for the Laminar Near Wake. Physics of Fluids, Vol. 19, 1970.

17. Roache, P.J. and Mueller, T.J.: Numerical Solutions of Compressible and Incompressible Separated Flows. AIAA Paper No. 68-747, 1968.

18. Victoria, K.J. and Steger, M.H.: Exact Solutions of the Two-Dimensional Laminar Near Wake of a Slender Body in Supersonic Flow at High Reynolds Number. Aerospace Company Report APP-0059 (S9990)-5, 1970.

19. Goodrich, W.D., Lamb, J.P. and Bertin, J.J.: On the Numerical Solution of Two-Dimensional Laminar Compressible Flows with Imbedded Shock Waves. ASME Paper No. 72-FE-7, 1972.

20. Ross, B.B. and Cheng, S.I.: The Application of Finite Difference Methods to the Supersonic Near Wake. AIAA Paper No. 72-115, 1972.

21. Brailovskaya, I.Y.: Flow in the Near Wake. Soviet Physics-Doklady, Vol. 16, 1971.

22. Mikhail, A.G., Hankey, W.L. and Shang, J.S.: Computation of a Supersonic Flow Past an Axisymmetric Nozzle Boattail with Jet Exhaust. AIAA Journal, Vol. 18, No. 8, August, 1980.

23. Rom, J. and Bober, L.J.: Calculation of the Pressure Distribution on Axisymmetric Boattails Including the Effects of Viscous Interactions and Exhaust Jets in Subsonic Flow. NASA TM X-3109, 1974.

24. Fong, M.C.: An Analysis of Plume-Induced Boundary Layer Separation. Journal of Spacecraft, Vol. 8, 1971.

25. Sinha, R., Zakkay, V. and Erdos, J.: Flow Field Analysis of Plumes of Two-Dimensional Underexpanded Jets by a Time-Dependent Method. AIAA Journal, Vol. 9, 1971.

26. Grossman, B. and Melnik, R.E.: The Numerical Computation of the Transonic Flow over Afterbodies Including the Effect of Jet-Plume Viscous Interactions. AIAA Paper 75-62, 1975.

27. Salas, H.D.: The Numerical Computation of Inviscid Plume Flow Fields. AIAA Paper 74-523, 1974.

28. Murman, E.M. and Cole, J.D.: Calculation of Plane Steady Transonic Flows. AIAA Journal, Vol. 9, 1971.

29. Jameson, A.: Iterative Solution of Transonic Flows over Airfoils and Wings, Including Flows at Mach 1. Communication on Pure and Applied Mathematics, Vol. 27, 1974.

30. Green, J.E., Weeks, D.J. and Broman, J.W.F.: Prediction of Turbulent Boundary Layers by a Lag Entrainment Method. RAE Technical Report 72231, 1973.

31. Briley, W.R. and McDonald, H.: Numerical Prediction of Incompressible Separation Bubbles. Journal of Fluid Mehcanics, Vol. 69, 1975.

32. Briley, W.R. and McDonald, H.: Solution of the Multidimensional Compressible Navier-Stokes Equations by a Generalized Implicit Method. Journal of Computational Physics, Vol. 24, 1977.

33. Briley, W.R., McDonald, H. and Gibeling, H.J.: Solution of the Multidimensional Compressible Navier-Stokes Equations by a Generalized Implicit Method. United Technologies Research Center Report R75-911363-15, January 1976.

34. Gibleing, H.J., McDonald, H. and Briley, W.R.: Development of a Three-Dimensional Combustor Flow Analysis, Vols. I and II: Theoretical Studies. Air Force Aeropropulsion Laboratory Report AFAPL-TR-75-59; Vol. I, July 1975; Vol. II, October 1976.

35. Douglas, J. and Gunn, J.E.: A General Formulation of Alternating Direction Methods. Numerische Math., Vol. 6, 1964.

36. Favre, A.: Equations des Gay Turbulents Compressibles. J. de Mecanique, Vol. 4, pp. 361-392, 1965.

37. Bradshaw, P. and Ferriss, D.H.: Calculation of Boundary-Layer Development Using the Turbulent Energy Equation: Compressible Flow on Adiabatic Walls. J. Fluid Mechanics, Vol. 46, Part 1, 1971, pp. 83-110.

38. Launder, B.E. and Spalding, D.B.: The Numerical Computation of Turbulent Flows. Computer Methods in Applied Mechanics and Engineering, Vol. 3, 1974.

39. Gibeling, H.J., Buggeln, R.C. and McDonald, H.: Development of a Two-Dimensional Implicit Interior Ballistics Code, U.S. Army Armament Research and Development Command, Ballistic Research Laboratory Report ARBRL-CR-00411, January 1980.

40. Jones, W.P. and Launder, B.E.: The Prediction of Laminarization with a Two-Equation Model of Turbulence. Int. J. Heat Mass Transfer, Vol. 15, 1972, p. 301.

41. Shamroth, S.J. and Gibeling, H.J.: A Compressible Solution of the Navier-Stokes Equations for Turbulent Flow About an Airfoil, NASA CR-3183, 1979.

42. McDonald, H. and Fish, R.W.: Practical Calculation of Transitional Boundary Layers. Int. J. Heat and Mass Transfer, Vol. 16, No. 9, 1973, pp. 1729-1744.

43. Shamroth, S.J. and McDonald, H.: Assessment of a Transitional Boundary Layer Theory at Low Hypersonic Mach Numbers. Int. J. Heat and Mass Transfer, Vol. 18, 1975, pp. 1277-1284.

44. Kreskovsky, J.P., Shamroth, S.J. and McDonald, H.: Application of a General Boundary Layer Analysis to Turbulent Boundary Layers Subjected to Strong Favorable Pressure Gradients. J. Fluid Eng., Vol. 97, June 1975, pp. 217-224.

45. McDonald, H. and Camarata, F.J.: An Extended Mixing Length Approach for Computing the Turbulent Boundary Layer Development, Proceedings Computation of Turbulent Boundary Layers - 1968 AFOSR-IFP Stanford Conference, Vol. 1, pp. 83-98, 1969.

46. Van Driest, E.R.: On Turbulent Flow Near a Wall. Journal of the Aeronautical Sciences, November 1956.

47. Thames, P.D. and Lombard, C.K.: Geometric Conservation Law and Its Application to Flow Computations on Moving Grids, AIAA Journal, Vol. 17, No. 10, 1979, p. 103

48. Roberts, G.O.: Computational Methods for Boundary Layer Problems. Proceedings of the 2nd International Conference on Numerical Methods in Fluid Dynamics. Springer-Verlag, New York, 1971.

49. Roache, P.J.: Computational Fluid Dynamics. Hermosa Publishers, Albuquerque, 1972.

50. Fox, L.: Some Experiments with Singularities in Linear Elliptic Partial Differential Equations. Proceedings of the Royal Society of London, Series A, 1971.

51. Fox, L. and Sankar, R.I.: Boundary Singularities in Linear Elliptic Differential Equations. Journal of the Institute of Applied Mathematics, Vol. 5, 1969.

52. Ladeveze, J. and Peyret, R.: Calcul Numerique d'une Solution avec Singularite des Equations de Navier-Stokes: Ecoulement Dans Un Canal Avec Variation Brusque de Section. Journal de Mechanique, Vol. 13, 1974.

53. Briley, W.R. and McDonald, H.: An Implicit Numerical Method for the Multi-dimensional Compressible Navier-Stokes Equations. United Aircraft Research Laboratories Report M911363-6, November 1973.

54. McDonald, H. and Briley, W.R.: Three-Dimensional Flow of a Viscous or Inviscid Gas. J. Comp. Physics, Vol. 19, No. 2, 1975, p. 150.

55. Weinberg, B.C. and McDonald, H.: Solution of Three-Dimensional Time-Dependent Viscous Flows, Part 1: Investigation of Candidate Algorithms, SRA Report R79-90004, Final Contractor's Report (NAS2-10016), 1979.

56. Thomas, P.D. and Lombard, C.K.: Geometric Conservation Law and its Application to Flow Computations on Moving Grids, AIAA Journal, Vol. 17, No. 10, 1979.

57. Badrinarayanan, M.A.: An Experimental Investigation of Base Flows at Supersonic Speeds, Journal of the Royal Aeronautical Society, Vol. 65, pp. 475-482, July 1961.

58. Settles, G.S., Baca, B.K., Williams, D.R. and Bogdonoff, S.M.: A Study of Reattachment of a Free Shear Layer in Compressible Turbulent Flow, AIAA Paper 80-1408, July 1980.

59. Gibeling, H. and McDonald, H.: Development of a Two-Dimensional Implicit Interior Ballistics Code, Final Contractor's Report (DAAK11-79-C-0098), December 1980.

60. Levy, R., Private Communication.

61. Buggeln, R.C., McDonald, H. Levy, R. and Kreskovsky, J.P.: Development of a Three-Dimensional Supersonic Inlet Flow Analysis, NASA CR 3218, January 1980.

62. Maise, G. and McDonald, H.: Mixing Length and Kinematic Eddy Viscosity in a Compressible Boundary Layer, AIAA Journal Vol. 6, No. 1, January 1968.

63. Shamroth, S.J., McDonald, H. and Briley, W.R.: A Navier-Stokes Solution for Transonic Flow Through a Cascade, SRA Report R81-920007-F, Final Contractor's Report (N00019-79-C-0558), January 1982.

64. Ames, W.F.: Numerical Methods for Partial Differential Equations. Barnes & Noble, Inc., New York, New York, 1969.

65. von Rosenberg, D.A.: Methods for the Numerical Solution of Partial Differential Equations. American Elsevier Publishing Co., Inc., New York, New York, 1969.

66. Douglas, J. and Jones, B.F.: On Predictor-Corrector Methods for Nonlinear Parabolic Differential Equations. Soc. for Indust. Appl. Math., Vol. 11, 1963, pp. 195-204.

67. Gourlay, A.R. and Morris, J.L.: Finite-Difference Methods for Nonlinear Hyperbolic Systems. Math. Comp., Vol. 22, 1968, pp. 28-39.

68. Richtmyer, R.D. and Morton, K.W.: Difference Methods for Initial Value Problems. Second Edition. Interscience Publishers, New York, New York, 1967.

69. Chorin, A.J.: Numerical Study of Thermal Convection in a Fluid Layer Heated from Below. AEC R&D Report TID-4500 (also New York Univ. Rpt. NYO-1480-61), 1966.

70. Bellman, R.E. and Kalaba, R.E.: Quasilinearization and Nonlinear Boundary-Value Problems. American Elsevier Publ. Co., Inc., New York, 1965.

71. Peacemen, D.W. and Rachford, H.H.: The Numerical Solution of Parabolic and Elliptic Differential Equations. Soc. for Indust. Appl. Math., Vol. 3, 1955, pp. 28-41.

72. Douglas, J.: On the Numerical Integration of $u_{xx} + u_{yy} = u_t$ by Implicit Methods. Soc. for Indust. Appl. Math., Vol. 3, 1955, pp. 42-65.

73. Mitchell, A.R.: Computational Methods in Partial Differential Equations, Wiley, New York, 1969.

74. Yananko, N.N.: The Method of Fractional Steps, Translation Edited by M. Holt. Springer-Verlag, New York, New York, 1971.

APPENDIX A

The governing conservation equations in cylindrical-polar coordinates are transformed using the Jacobian transformation,

$$y^j = y^j(\bar{x}_1, \bar{x}_2, \bar{x}_3, t)$$
$$\tau = t \tag{A-1}$$

where $(\bar{x}_1, \bar{x}_2, \bar{x}_3) = (r, \theta, z)$. The resulting equations may be written in the following compact form:

$$\frac{\partial(J\vec{W})}{\partial\tau} = -\sum_{j=1}^{3}\left\{\frac{\partial}{\partial y^j}(J y^j_{,t}\vec{W}) + \sum_{i=1}^{3}\left[\beta_i \frac{\partial}{\partial y^j}(J y^j_{,i}\vec{F}_i)\right.\right.$$
$$\left.\left. -\zeta_i \frac{\partial}{\partial y^j}(J y^j_{,i}\vec{G}_i)\right]\right\} + J\vec{S} + J\vec{C} \tag{A-2}$$

where

$$y^j_{,t} \equiv \frac{\partial y^j}{\partial t}$$
$$y^j_{,i} \equiv \frac{\partial y^j}{\partial \bar{x}_i} \tag{A-3}$$

Further, the coefficients β_i, γ_i, ζ_i are given by

$$\beta_1 = \frac{1}{r}, \quad \beta_2 = \frac{1}{r}, \quad \beta_3 = 1$$
$$\gamma_1 = 1, \quad \gamma_2 = \frac{1}{r}, \quad \gamma_3 = 1 \tag{A-4}$$
$$\zeta_1 = \frac{1}{r^m}, \quad \zeta_2 = \frac{1}{r}, \quad \zeta_3 = 1$$

and $m = 1$ for all equations except the $\bar{x}_2$-direction momentum equations for which $m = 2$.

The vector variables used in Eq. (A-2) are defined as

$$\vec{W} = \begin{bmatrix} \rho U_1 \\ \rho U_2 \\ \rho U_3 \\ \rho \\ \rho h \\ \rho k \end{bmatrix} \qquad (A\text{-}5)$$

$$\vec{F}_i = r^n \begin{bmatrix} \rho U_1 U_i \\ \rho U_2 U_1 \\ \rho U_3 U_i \\ \rho U_i \\ \rho h U_i \\ \rho k U_i \end{bmatrix} \qquad (A\text{-}6)$$

where n = 1 for i = 1 and n = 0 for i = 2, 3.

$$\vec{G}_1 = \begin{bmatrix} r\tau_{11} \\ r^2\tau_{12} \\ r\tau_{13} \\ 0 \\ -rq_1 \\ \frac{\mu_T}{\sigma_k}\gamma_1 k_{,1} \end{bmatrix} \qquad (A\text{-}7)$$

$$\vec{G}_i = \begin{bmatrix} \tau_{i1} \\ \tau_{i2} \\ \tau_{i3} \\ 0 \\ -q_i \\ \frac{\mu_T}{\sigma_k}\gamma_i k_{,i} \end{bmatrix} \quad \text{for} \quad i = 2,3 \qquad (A\text{-}8)$$

Note that the velocity components (U_1, U_2, U_3) are the cylindrical-polar velocity components written in cylindrical-polar coordinates. The molecular and turbulent stress tensors, Eqs. (6) and (8), may be written as

$$\tau_{ij} = 2\mu_{eff}\bar{D}_{ij} - \frac{2}{3}\mu_{eff}(\nabla\cdot\vec{U})\delta_{ij} + \frac{2}{3}(K_B\nabla\cdot\vec{U} - \rho k)\delta_{ij} \qquad (A\text{-}9)$$

and the rate of strain tensor components in cylindrical-polar coordinates are

$$\bar{D}_{11} = \frac{\partial U_1}{\partial \bar{x}_1}$$

$$\bar{D}_{22} = \frac{1}{r}\frac{\partial U_2}{\partial \bar{x}_2} + \frac{U_1}{r}$$

$$\bar{D}_{33} = \frac{\partial U_3}{\partial \bar{x}_3} \qquad \text{(A-10)}$$

$$\bar{D}_{12} = \frac{1}{2}\left[r\frac{\partial}{\partial \bar{x}_1}\left(\frac{U_2}{r}\right) + \frac{1}{r}\frac{\partial U_1}{\partial \bar{x}_2} \right]$$

$$\bar{D}_{13} = \frac{1}{2}\left[\frac{\partial U_3}{\partial \bar{x}_1} + \frac{\partial U_1}{\partial \bar{x}_3} \right]$$

$$\bar{D}_{23} = \frac{1}{2}\left[\frac{1}{r}\frac{\partial U_3}{\partial \bar{x}_2} + \frac{\partial U_2}{\partial \bar{x}_3} \right]$$

and

$$\nabla \cdot \vec{U} = \frac{1}{r}\frac{\partial}{\partial \bar{x}_1}(r U_1) + \frac{1}{r}\frac{\partial U_2}{\partial \bar{x}_2} + \frac{\partial U_3}{\partial \bar{x}_3} \qquad \text{(A-11)}$$

The derivatives required in Eqs. (A-10 and A-11) must be expressed in terms of the computational coordinates y^j using the chain rule, Eq. (34).

Finally, the vector $\vec{S}$ contains source terms and certain differential terms which do not conform to the basic structure of Eq. (A-2), and the vector $\vec{C}$ contains the additional curvature terms due to the cylindrical-polar coordinate system.

$$\vec{S} = \begin{bmatrix} 0 \\ 0 \\ 0 \\ 0 \\ \frac{D(\rho)}{Dt} + \Phi + \rho\epsilon \\ \left\{ \mu_T \left[2\bar{D}_{ij}\bar{D}_{ij} - \frac{2}{3}(\nabla\cdot\vec{U})^2 \right] - \frac{2}{3}\rho k \nabla\cdot\vec{U} - \rho\epsilon \right\} + S_k \end{bmatrix} \qquad \text{(A-12)}$$

$$\bar{\bar{C}} = \begin{bmatrix} \frac{1}{r} \rho U_2^2 - \frac{1}{r} \bar{\tau}_{22} \\ -\frac{1}{r} \rho U_1 U_2 \\ 0 \\ 0 \\ 0 \\ 0 \end{bmatrix} \qquad \text{(A-13)}$$

APPENDIX B

Linearization Technique

A number of techniques have been used for implicit solution of the following first-order nonlinear scalar equation in one dependent variable $\phi(x,t)$:

$$\partial\phi/\partial t = F(\phi)\,\partial G(\phi)/\partial x \qquad \text{(B1)}$$

Special cases of Eq. (B1) include the conservation form if $F(\phi) = 1$, and quasi-linear flow if $G(\phi) = \phi$. Previous implicit methods for Eq. (B1) which employ nonlinear difference equations and also methods based on two-step predictor-corrector schemes are discussed by Ames (Ref. 64, p. 82) and von Rosenburg (Ref. 65), p. 56). One such method is to difference nonlinear terms directly at the implicit time level to obtain nonlinear implicit difference equations; these are then solved iteratively by a procedure such as Newton's method. Although otherwise attractive, there may be difficulty with convergence in the iterative solution of the nonlinear difference equations, and some efficiency is sacrificed by the need for iteration. An implicit predictor-corrector technique has been devised by Douglas and Jones (Ref. 66) which is applicable to the quasilinear case ($G = \phi$) of Eq. (B1). The first step of their procedure is to linearize the equation by evaluating the non-linear coefficient as $F(\phi^n)$. and to predict values of $\phi^{n+1/2}$ using either the backward difference or the Crank-Nicolson scheme. Values for ϕ^{n+1} are then computed in a similar manner using $F(\phi^{n+1/2})$ and the Crank-Nicolson scheme. Gourlay and Morris (Ref. 67) have also proposed implicit predictor-corrector techniques which can be applied to Eq. (A1). In the conservative case (F=1), their technique is to define $\hat{G}(\phi)$ by the relation $G(\phi) = \phi\hat{G}(\phi)$ when such a definition exists, and to evaluate $\hat{G}(\phi^{n+1})$ using the values for ϕ^{n+1} computed by an explicit predictor scheme. With $\hat{G}$ thereby known at the implicit time level, the equation can be treated as linear and corrected values of ϕ^{n+1} are computed by the Crank-Nicolson scheme.

A technique is described here for deriving linear implicit difference approximations for nonlinear differential equations. The technique is based on an expansion of nonlinear implicit terms about the solution at the known time

level, t^n, and leads to a one-step, two-level scheme which, being linear in unknown (implicit) quantities, can be solved efficiently without iteration. This idea was applied by Richtmyer and Morton (Ref. 68, p. 203) to a scalar nonlinear diffusion equation. Here, the technique is developed for problems governed by ℓ nonlinear equations in ℓ dependent variables which are functions of time and space coordinates. Although the present effort concentrates upon two spatial dimensions and time, the technique will be described for the three-dimensional, unsteady equations.

The solution domain is discretized by grid points having equal spacings in the computational coordinates, Δy^1, Δy^2 and Δy^3 in the y^1, y^2 and y^3 directions, respectively, and an arbitrary time step, Δt. The subscripts i, j, k and superscript n are grid point indices associated with y^1, y^2, y^3 and t, respectively, and thus $\phi^n_{i,j,k}$ denotes $\phi(y^1_i, y^2_j, y^3_k, t^n)$. It is assumed that the solution is known at the n level, t^n, and is desired at the (n+1) level, t^{n+1}. At the risk of an occasional ambiguity, one or more of the subscripts is frequently omitted, so that ϕ^n is equivalent to $\phi^n_{i,j,k}$.

Although present attention is focused on the compressible Navier-Stokes equations, the numerical method employed is quite general and is formally derived for systems of governing equations which have the following form:

$$\partial H(\phi)/\partial t = \mathcal{D}(\phi) + S(\phi) \tag{B2}$$

where ϕ is a column vector containing ℓ dependent variables, H and S are column vector functions of ϕ, and $\mathcal{D}$ is a column vector whose elements are spatial differential operators which may be multidimensional. The generality of Eq. (B2) allows the method to be developed concisely and permits various extensions and modifications (e.g., noncartesian coordinate systems, turbulence models) to be made more or less routinely. It should be emphasized, however, that the Jacobian $\partial H/\partial\phi$ must usually be nonsingular if the ADI techniques as applied to Eq. (B2) are to be valid. A necessary condition is that each dependent variable appear in one or more of the governing equations as a time derivative. An exception would occur if for instance, a variable having no time

derivative also appeared in only one equation, so that this equation could be decoupled from the remaining equations and solved a posteriori by an alternate method. As a consequence, the present method is not directly applicable to the incompressible Navier-Stokes equations except in one-dimension, where ADI techniques are unnecessary. For example, the velocity-pressure form of the incompressible equations has no time derivative of pressure, whereas the vorticity-stream-function form has no time derivative of stream function. For computing steady solutions, however, the addition of suitable "artificial" time derivatives to the incompressible equations, as was done in Chorin's (Ref. 69) artificial compressibility method, would permit the application of the present method. Alternatively, a low Mach number solution of the compressible equations can be computed.

The linearized difference approximation is derived from the following implicit time-difference replacement of Eq. (B2):

$$(H^{n+1}-H^{n})/\Delta t=\beta\left[\mathcal{D}(\phi^{n+1})+S^{n+1}\right]+(1-\beta)\left[\mathcal{D}(\phi^{n})+S^{n}\right] \tag{B3}$$

where, for example, $H^{n+1}\equiv H(\phi^{n+1})$. The form of $\mathcal{D}$ and the spatial differencing are as yet unspecified. A parameter $\beta(0 \leq \beta \leq 1)$ has been introduced so as to permit a variable centering of the scheme in time. Equation (B3) produces a backward difference formulation for $\beta = 1$ and a Crank-Nicolson formulation for $\beta = 1/2$.

The linearization is performed by a two-step process of expansion about the known time level t^n and subsequent approximation of the quantity $(\partial\phi/\partial t)^n\Delta t$, which arises from chain rule differentiation, by $(\phi^{n+1}-\phi^{n})$. The result is

$$H^{n+1}=H^{n}+(\partial H/\partial\phi)^{n}(\phi^{n+1}-\phi^{n})+O(\Delta t)^{2} \tag{B4a}$$

$$S^{n+1}=S^{n}+(\partial S/\partial\phi)^{n}(\phi^{n+1}-\phi^{n})+O(\Delta t)^{2} \tag{B4b}$$

$$\mathcal{D}(\phi^{n+1}) = \mathcal{D}(\phi^n) + (\partial \mathcal{D}/\partial\phi)^n(\phi^{n+1}-\phi^n) + O(\Delta t)^2 \qquad \text{(B4c)}$$

The matrices $\partial H/\partial\phi$ and $\partial S/\partial\phi$ are standard Jacobians whose elements are defined, for example, by $(\partial H/\partial\phi)_{qr} \equiv \partial H_q/\partial\phi_r$. The operator elements of the matrix $\partial\mathcal{D}/\partial\phi$ are similarly ordered, i.e., $(\partial\mathcal{D}/\partial\phi)_{qr} \equiv \partial\mathcal{D}_q/\partial\phi_r$; however, the intended meaning of the operator elements requires some clarification. For the q^{th} row, the operation $(\partial\mathcal{D}_q/\partial\phi)^n\ (\phi^{n+1} - \phi^n)$ is understood to mean that $\{\partial/\partial t\,\mathcal{D}_q[\phi(x,y,z,t)]\}^n\ \Delta t$ is computed and that all occurrences of $(\partial\phi_r/\partial t)^n$ arising from chain rule differentiation are replaced by $(\phi_r^{n+1} - \phi_r^n)/\Delta t$.

After linearization as in Eqs. (B4), Eq. (A3) becomes the following linear implicit time-differenced scheme:

$$(\partial H^n/\partial\phi)(\phi^{n+1}-\phi^n)/\Delta t = \mathcal{D}(\phi^n) + S^n + \beta\,(\partial\mathcal{D}/\partial\phi + \partial S^n/\partial\phi)(\phi^{n+1}-\phi^n) \qquad \text{(B5)}$$

Although H^{n+1} is linearized to second order in Eq. (B4), the division by Δt in Eq. (B3) introduces an error term of order Δt. A technique for maintaining formal second-order accuracy in the presence of nonlinear time derivatives is discussed by McDonald and Briley (Ref. 32), however, a three-level scheme results. Second-order temporal accuracy can also be obtained (for $\beta = 1/2$) by a change in dependent variable to $\hat{\phi} \equiv H(\phi)$, provided this is convenient, since the nonlinear time derivative is then eliminated. The temporal accuracy is independent of the spatial accuracy.

On examination, it can be seen that Eq. (B5) is linear in the quantity $(\phi^{n+1} - \phi^n)$ and that all other quantities are either known or evaluated at the n level. Computationally, it is convenient to solve Eq. (B5) for $(\phi^{n+1} - \phi^n)$ rather than ϕ^{n+1}. This both simplifies Eq. (B5) and reduces roundoff errors, since it is presumably better to compute a small $O(\Delta t)$ change in an $O(1)$ quantity than the quantity itself. To simplify the notation, a new dependent variable ψ defined by

$$\psi \equiv \phi - \phi^n \qquad \text{(B6)}$$

is introduced, and thus $\psi^{n+1} = \phi^{n+1} - \phi^n$, and $\psi^n = 0$. It is also convenient to rewrite Eq. (A5) in the following simplified form:

$$(A + \Delta t\, \mathcal{L})\psi^{n+1} = \Delta t \left[\mathcal{D}(\phi^n) + S^n\right] \tag{B7a}$$

where the following symbols have been introduced to simplify the notation:

$$A \equiv \partial H^n / \partial \phi - \beta \Delta t (\partial S^n / \partial \phi) \tag{B7b}$$

$$\mathcal{L} \equiv -\beta (\partial \mathcal{D} / \partial \phi) \tag{B7c}$$

It is noted that $\mathcal{L}(\psi)$ is a linear transformation and thus $\mathcal{L}(0) = 0$. Furthermore, if $\mathcal{D}(\phi)$ is linear, then $\mathcal{L}(\psi) = -\beta\, \mathcal{D}(\psi)$.

Spatial differencing of Eq. (B7a) is accomplished simply by replacing derivative operators such as $\partial/\partial y^i$, $\partial^2/\partial y^i \partial y^i$ by corresponding finite difference operators, D_i, D_i^2. Henceforth, it is assumed that $\mathcal{D}$ and $\mathcal{L}$ have been discretized in this manner, unless otherwise noted.

Before proceeding, some general observations seem appropriate. The foregoing linearization technique assumes only Taylor expandability, an assumption already implicit in the use of a finite difference method. The governing equations and boundary conditions are addressed directly as a system of coupled nonlinear equations which collectively determine the solution. The approach thus seems more natural than that of making <u>ad hoc</u> linearization and decoupling approximations, as is often done in applying implicit schemes to coupled and/or nonlinear partial differential equations. With the present approach, it is not necessary to associate each governing equation and boundary condition with a particular dependent variable and then to identify various "nonlinear coefficients" and "coupling terms" which must then be treated by lagging, predictor-corrector techniques, or iteration. The Taylor expansion procedure is analogous to that used in the generalized Newton-Raphson or quasi-linearization

methods for iterative solution of nonlinear systems by expansion about a known current guess at the solution (e.g., Bellman & Kalaba, Ref. 70). However, the concept of expanding about the previous time level apparently had not been employed to produce a noniterative implicit time-dependent scheme for coupled equations, wherein nonlinear terms are approximated to a level of accuracy commensurate with that of the time differencing. The linearization technique also permits the implicit treatment of coupled nonlinear boundary conditions, such as stagnation pressure and enthalpy at subsonic inlet boundaries, and in practice, this latter feature was found to be crucial to the stability of the overall method (Ref. 32).

Application of Alternating-Direction Techniques

Solution of Eq. (B7a) is accomplished by application of an alternating-direction implicit (ADI) technique for parabolic-hyperbolic equations. The original ADI method was introduced by Peaceman and Rachford (Ref. 71) and Douglas (Ref. 72); however, the alternating-direction concept has since been expanded and generalized. A discussion of various alternating-direction techniques is given by Mitchell (Ref. 73) and Yanenko (Ref. 74).

The present technique is simply an application of the very general procedure developed by Douglas and Gunn (Ref. 35) for generating ADI schemes as perturbations of fundamental implicit difference schemes such as the backward-difference or Crank-Nicolson schemes.

For the present, it will be assumed that $\mathcal{D}(\phi)$ contains derivatives of first and second order with respect to y^1, y^2 and y^3, but no mixed derivatives. In this case, $\mathcal{D}$ can be split into three operators, $\mathcal{D}_1, \mathcal{D}_2, \mathcal{D}_3$ associated with the y^1, y^2 and y^3 coordinates and each having the functional form $\mathcal{D}_i = \mathcal{G}(\phi, \partial/\partial y^i, \partial^2/\partial y^i \partial y^i)$. Equation (A7a) then becomes

$$\left[A+\Delta t(\mathcal{L}_1 + \mathcal{L}_2 + \mathcal{L}_3)\right]\psi^{n+1} = \Delta t\left[(\mathcal{D}_1 + \mathcal{D}_2 + \mathcal{D}_3)\phi^n + S^n\right] \qquad (B8)$$

Recalling that $\mathcal{L}(\psi^n) = 0$, the Douglas-Gunn representation of Eq. (B8) can be written as the following three-step solution procedure:

$$(A+\Delta t\,\mathcal{L}_1)\psi^* = \Delta t\left[(\mathcal{D}_1+\mathcal{D}_2+\mathcal{D}_3)\phi^n + S^n\right] \tag{B9a}$$

$$(A+\Delta t\,\mathcal{L}_2)\psi^{**} = A\psi^* \tag{B9b}$$

$$(A+\Delta t\,\mathcal{L}_3)\psi^{n+1} = A\psi^{**} \tag{B9c}$$

where ψ^* and ψ^{**} are intermediate solutions. It will be shown subsequently that each of Eqs. (B9) can be written in narrow block-banded matrix form and solved by efficient block-elimination methods. If ψ^* and ψ^{**} are eliminated, Eqs. (B9) become

$$(A+\Delta t\,\mathcal{L}_1)A^{-1}(A+\Delta t\,\mathcal{L}_2)A^{-1}(A+\Delta t\,\mathcal{L}_3)\psi^{n+1} = \Delta t\left[(\mathcal{D}_1+\mathcal{D}_2+\mathcal{D}_3)\phi^n + S^n\right] \tag{B10}$$

If the multiplication on the left-hand side of Eq. (B10) is performed, it becomes apparent that Eq. (B10) approximates Eq. (B8) to order $(\Delta t)^2$. Although the stability of Eqs. (B9) has not been established in circumstances sufficiently general to encompass the Navier-Stokes equations, it is often suggested (e.g., Richtmyer & Morton, Ref. 68, p. 215) that the scheme is stable and accurate under conditions more general than those for which rigorous proofs are available. This latter notion was adopted here as a working hypothesis supported by favorable results obtained in actual computations (e.g., Refs. 33 and 34).

A major attraction of the Douglas-Gunn scheme is that the intermediate solutions ψ^* and ψ^{**} are consistent approximations to ψ^{n+1}. Furthermore, for steady solutions, $\psi^n = \psi^* = \psi^{**} = \psi^{n+1}$ independent of Δt. Thus, physical boundary conditions for ψ^{n+1} can be used in the intermediate steps without a serious loss in accuracy and with no loss for steady solutions. In this respect, the Douglas-Gunn scheme appears to have an advantage over locally one-dimensional (LOD) or "splitting" schemes, and other schemes whose intermediate steps do not satisfy the consistency condition. The lack of consistency in the intermediate steps complicates the treatment of boundary conditions and, according to Yanenko

(Ref. 74, p. 33), does not permit the use of asymptotically large time steps. It is not clear that this advantage of the Douglas-Gunn scheme would always outweigh other benefits which might be derived from an alternative scheme. However, since the ADI scheme can be viewed as an approximate technique for solving the fundamental difference scheme, Eq. (B7a), alternate techniques can readily be used within the present formulation.

It is worth noting that the operator $\mathcal{D}$ can be split into any number of components which need not be associated with a particular coordinate direction. As pointed out by Douglas and Gunn (Ref. 41), the criterion for identifying sub-operators is that the associated matrices be "easily solved" (i.e., narrow-banded). Thus, mixed derivatives can be treated implicitly within the ADI framework, although this would increase the number of intermediate steps and thereby complicate the solution procedure. Finally, only minor changes are introduced if, in the foregoing development of the numerical method, H, $\mathcal{D}$, and S are functions of the spatial coordinates and time, as well as ϕ.


DATE
FILME
7-8